symmetry

MDPI

Article

Nuclear Matter and Finite Nuclei: Recent Studies Based on Parity Doublet Model

Yuk-Kei Kong [1,*,†], Youngman Kim [2,*,†] and Masayasu Harada [1,3,4,*,†]

[1] Department of Physics, Nagoya University, Nagoya 464-8602, Japan
[2] Center for Exotic Nuclear Studies, Institute for Basic Science, Daejeon 34126, Republic of Korea
[3] Kobayashi-Maskawa Institute for the Origin of Particles and the Universe, Nagoya University, Nagoya 464-8602, Japan
[4] Advanced Science Research Center, Japan Atomic Energy Agency, Tokai 319-1195, Japan
* Correspondence: yukkekong2-c@hken.phys.nagoya-u.ac.jp (Y.-K.K.); ykim@ibs.re.kr (Y.K.); harada@hken.phys.nagoya-u.ac.jp (M.H.)
† These authors contributed equally to this work.

Abstract: In this review, we summarize recent studies on nuclear matter and finite nuclei based on parity doublet models. We first construct a parity doublet model (PDM), which includes the chiral invariant mass m_0 of nucleons together with the mass generated by the spontaneous chiral symmetry breaking. We then study the density dependence of the symmetry energy in the PDM, which shows that the symmetry energy is larger for smaller chiral inavariant mass. Then, we investigate some finite nuclei by applying the Relativistic Continuum Hartree–Bogoliubov (RCHB) theory to the PDM. We present the root-mean-square deviation (RMSD) of the binding energies and charge radii, and show that $m_0 = 700$ MeV is preferred by the nuclear properties. Finally, we modify the PDM by adding the isovector scalar meson $a_0(980)$, and show that the inclusion of the $a_0(980)$ enlarges the symmetry energy of the infinite nuclear matter.

Keywords: parity doublet model; chiral invariant mass; isovector scalar meson; finite nuclei; nuclear matter; symmetry energy

Citation: Kong, Y.-K.; Kim, Y.; Harada, M. Nuclear Matter and Finite Nuclei: Recent Studies Based on Parity Doublet Model. *Symmetry* **2024**, *16*, 1238. https://doi.org/10.3390/sym16091238

Academic Editors: Marcello Abbrescia and Stefano Profumo

Received: 2 May 2024
Revised: 17 August 2024
Accepted: 9 September 2024
Published: 20 September 2024

1. Introduction

Spontaneous chiral symmetry breaking plays an important role in low-energy hadron physics, contributing substantially to the generation of hadron masses and the manifestation of mass differences between chiral partners. In recent decades, there has been a growing focus on investigating the restoration of chiral symmetry in hot and dense matter. Nucleon masses will be changed in such extreme conditions, which provides hints for us towards a further understanding to the mass of hadrons and further understanding to the dynamics of the strongly interacting matter.

In the traditional linear sigma model, the entire nucleon mass is generated from the spontaneous chiral symmetry breaking, in which the chiral partner to ordinary nucleon is the nucleon itself. When the chiral symmetry is restored, the nucleon and its chiral partner will be degenerate in mass. However, increasing evidence from the lattice calculations [1,2] show that, with increasing temperature, the mass of negative parity baryon decreases to be degenerate with the mass of positive baryon at the critical temperature.

The Parity Doublet Model (PDM) was proposed in Ref. [3] as an extended linear sigma model with parity doubling structure to model the parity doubling of nucleon. In the PDM, the excited nucleon, such as $N(1535)$, is regarded as the chiral partner to the ordinary nucleon, in which the spontaneous symmetry breaking generates the mass difference between them. By considering the symmetry properties of the chiral partner, the PDM predicts that the masses of the parity partners are degenerate into a finite mass, the so-called chiral invariant mass m_0, when the chiral symmetry is restored. In addition to the

lattice simulations mentioned above, a recent analysis based on the QCD sum rules [4] also supports the existence of the chiral invariant mass. Therefore, quantitative and qualitative study of the chiral invariant mass will help us to understand the origin of hadron masses.

Studying the chiral invariant mass m_0 is an essential measure to the origin of the mass of a nucleon. There are several analyses to determine the value of m_0 by studying the nucleon properties in vacuum. For example, the analysis in Ref. [5] shows that m_0 is smaller than 500 MeV using the decay width of $N(1535)$, while Ref. [6] includes higher derivative interaction, which makes the large m_0 consistent with the decay width.

Chiral symmetry is expected to be partially restored in the high density region, the study of which will provide some information on the chiral invariant mass. Actually, the PDM is applied to study high density matter in several analyses, such as in Refs. [7–40]. Recently, in Refs. [33,35,37,38,40], the EoS of neutron star (NS) matter constructed from an extended PDM [19] was connected to the one from the NJL-type quark model, following Refs. [41,42]. The analysis of Ref. [33] used the observational data of NS given in Refs. [43–48] to put a constraint on the chiral invariant mass m_0 as 600 MeV $\lesssim m_0 \lesssim$ 900 MeV, which was updated in Refs. [37,38] to 400 MeV$\lesssim m_0 \lesssim$ 700 MeV by considering the effect of anomaly, as well as new data analysis [49–51]. Ref. [40] showed that $m_0 \simeq$ 850 MeV with the consideration of central compact object (CCO) within the supernova remnant HESS J1731-347 [52].

In recent decades, increasing attention is paid to the effect of isovector-scalar $a_0(980)$ meson (also called the δ meson) on asymmetric matter such as NS because it accounts for the attractive force in the isovector channel. References [53–63] use Walecka-type relativistic mean-field (RMF) models, and Refs. [64,65] use density-dependent RMF models to study the effect of $a_0(980)$ meson to the symmetry energy as well as to the EoS of asymmetric matter. It was pointed that the existence of a_0 meson increases the symmetry energy [53,55,56,59–63], and that it stiffens the NS EoS [54–56,58,59] and asymmetric matter EoS [65]. Therefore, the $a_0(980)$ meson is influential for the study of asymmetric matter. Recently, in Ref. [66], the effect of $a_0(980)$ in neutron star is studied in the PDM and the constraint to the chiral invariant mass is obtained as 580 MeV $\lesssim m_0 \lesssim$ 860 MeV. In particular, this work shows that the $a_0(980)$ meson has large influence to the symmetry energy at density larger than saturation density. Therefore, it is expected that further experimental constraints on the symmetry energy will provide hints to the chiral invariant mass and the origin of the mass of a nucleon.

To put an additional constraint on the value of the chiral invariant mass, the properties of stable nuclei were studied in Ref. [67] with the PDM in the frame work of a self-consistent relativistic mean field theory. For the nuclear structure calculations, the Relativistic Continuum Hartree–Bogoliubov (RCHB) theory [68] was employed. It was found in Ref. [67] that the calculated binding energies and charge radii of selected fifteen nuclei are closest to the experimental values when $m_0 = 700$ MeV.

In this review, we summarize the recent works on the study of chiral invariant mass in infinite nuclear matter in Ref. [66] and finite nuclei in Ref. [67]. In Section 2.1, we introduce a PDM including a_0 meson based on the chiral $\mathrm{U}(2)_L \times \mathrm{U}(2)_R$ symmetry with $\mathrm{U}(1)_A$ anomaly included. Then, as a first step, we drop the a_0 meson and construct the infinite nuclear matter using mean field approximation in Sections 2.2–2.4. In Section 3, the construction of finite nuclei in mean field model using Relativistic Continuum Hartree–Bogoliubov (RCHB) theory is introduced. After a brief introduction on the construction of finite nuclei, the finite nuclei are constructed using PDM, as in Ref. [67], and the method to constrain the value of chiral invariant mass using experimental data of finite nuclei are discussed. Some results on the specific nuclei, such as the nuclei properties and effective mass of a nucleon in finite nuclei, are also shown. In Section 4, we review an extension of the PDM by including the isovector scalar meson $a_0(980)$ performed in Ref. [66]. We also compute the results for the extended PDM without vector meson mixing interaction for comparison. The symmetry energy for these models are compared to the PDM without a_0 meson introduced in Section 2. Finally, a summary is given in Section 5.

2. Dense Nuclear Matter with Parity Doublet Model

2.1. A Parity Doublet Model with $U(2)_L \times U(2)_R$ Symmetry

Here, we introduce the parity doublet model (PDM) based on the $\mathrm{U}(2)_L \times \mathrm{U}(2)_R$ chiral symmetry constructed in Ref. [66]. The Lagrangian is given by

$$\mathcal{L} = \mathcal{L}_N + \mathcal{L}_M + \mathcal{L}_V \,, \tag{1}$$

where $\mathcal{L}_N$ is for the nucleons, $\mathcal{L}_M$ for the scalar and pseudoscalar mesons and $\mathcal{L}_V$ for the vector mesons.

In $\mathcal{L}_M$, the scalar meson field M is introduced as the $(2,2)_{-2}$ representation under the $\mathrm{SU}(2)_L \times \mathrm{SU}(2)_R \times \mathrm{U}(1)_A$ symmetry, which transforms as

$$M \to e^{-2i\theta_A} g_L M g_R^\dagger \,, \tag{2}$$

where $g_{R,L} \in \mathrm{SU}(2)_{R,L}$ and $e^{-2i\theta_A} \in \mathrm{U}(1)_A$. We parameterize M as

$$M = [\sigma + i\vec{\pi}\cdot\vec{\tau}] - [\vec{a_0}\cdot\vec{\tau} + i\eta] \,, \tag{3}$$

where $\sigma, \vec{\pi}, \vec{a_0}, \eta$ are fields for the sigma meson, pions, the lightest isovector scalar meson $a_0(980)$ and η meson, respectively, and $\vec{\tau}$ are the Pauli matrices. The vacuum expectation value (VEV) of M is

$$\langle 0|M|0\rangle = \begin{pmatrix} \sigma_0 & 0 \\ 0 & \sigma_0 \end{pmatrix}, \tag{4}$$

where $\sigma_0 = \langle 0|\sigma|0\rangle$ is the VEV of the σ field, which is equal to the pion decay constant $f_\pi = 93$ MeV in vacuum. The explicit form of the Lagrangian $\mathcal{L}_M$ is given by

$$\mathcal{L}_M = \frac{1}{4}\mathrm{tr}\left[\partial_\mu M \partial^\mu M^\dagger\right] - V_M \,, \tag{5}$$

where V_M is the potential for M. In the present model, V_M is taken as [66]

$$\begin{aligned} V_M = &-\frac{\bar{\mu}^2}{4}\mathrm{tr}[M^\dagger M] + \frac{\lambda_{41}}{8}\mathrm{tr}[(M^\dagger M)^2] \\ &- \frac{\lambda_{42}}{16}\{\mathrm{tr}[M^\dagger M]\}^2 - \frac{\lambda_{61}}{12}\mathrm{tr}[(M^\dagger M)^3] \\ &- \frac{\lambda_{62}}{24}\mathrm{tr}[(M^\dagger M)^2]\mathrm{tr}[M^\dagger M] - \frac{\lambda_{63}}{48}\{\mathrm{tr}[M^\dagger M]\}^3 \\ &- \frac{m_\pi^2 f_\pi}{4}\mathrm{tr}[M + M^\dagger] - \frac{K}{8}\{\det M + \det M^\dagger\} \,, \end{aligned} \tag{6}$$

where we included all the terms invariant under $\mathrm{SU}(2)_L \times \mathrm{SU}(2)_R \times \mathrm{U}(1)_A$ symmetry up to the sixth order in M fields. The six-point interaction terms are introduced to reproduce the nuclear saturation properties following Ref. [19]. The term proportional to m_π^2 is the explicit chiral symmetry breaking term due to the non-zero current quark masses, which generates the mass of pion. The last term is introduced to account for the $\mathrm{U}(1)_A$ anomaly.

For vector mesons, the iso-triplet ρ meson and iso-singlet ω meson are included based on the hidden local symmetry (HLS) [69–71] to account for the repulsive force in the hadronic matter. The HLS is introduced by performing polar decomposition of the field M as

$$M = \xi_L^\dagger S \xi_R \,, \tag{7}$$

where $S = \sigma + \sum_{b=1}^{3} a_0^b \tau_b/2$ is the 2×2 matrix field for scalar mesons. The fields $\xi_{L,R}$ transform as

$$\xi_{L,R} \to h_\omega h_\rho \xi_{L,R} g_{L,R}^\dagger e^{\pm i\theta_A}, \tag{8}$$

with $h_\omega \in \mathrm{U}(1)_{\mathrm{HLS}}$ and $h_\rho \in \mathrm{SU}(2)_{\mathrm{HLS}}$. Here, $e^{+i\theta_A}$ for ξ_L and $e^{-i\theta_A}$ for ξ_R. In the unitary gauge of the HLS, $\xi_{L,R}$ are parameterized as

$$\xi_R = \xi_L^\dagger = \exp(iP/f_\pi)\,, \tag{9}$$

where $P = \eta + \sum_{a=1}^{3} \pi^a \tau_a/2$ is the 2×2 matrix field for pseudoscalar mesons. In the HLS, vector mesons are introduced as the gauge bosons of the HLS. They transform as

$$\omega_\mu \to h_\omega \omega_\mu h_\omega^\dagger + \frac{i}{g_\omega}\partial_\mu h_\omega h_\omega^\dagger, \tag{10}$$

$$\rho_\mu \to h_\rho \rho_\mu h_\rho^\dagger + \frac{i}{g_\rho}\partial_\mu h_\rho h_\rho^\dagger, \tag{11}$$

where ω_μ and $\rho_\mu = \sum_{a=1}^{3} \rho_\mu^a \tau_a/2$ are the gauge fields for $\mathrm{SU}(2)_{\mathrm{HLS}}$ and $\mathrm{U}(1)_{\mathrm{HLS}}$, respectively, and g_ω and g_ρ are the corresponding gauge coupling constants.

To construct the Lagrangian invariant under the HLS, it is convenient to define the covariantized Maurer–Cartan 1-forms:

$$\hat{\alpha}_\perp^\mu \equiv \frac{1}{2i}[D^\mu \xi_R \xi_R^\dagger - D^\mu \xi_L \xi_L^\dagger], \tag{12}$$

$$\hat{\alpha}_\parallel^\mu \equiv \frac{1}{2i}[D^\mu \xi_R \xi_R^\dagger + D^\mu \xi_L \xi_L^\dagger], \tag{13}$$

where the covariant derivatives of $\xi_{L,R}$ are given by

$$D^\mu \xi_L = \partial^\mu \xi_L - i g_\rho \rho^\mu \xi_L - i g_\omega \omega^\mu \xi_L + i \xi_L \mathcal{L}^\mu - i \xi_L \mathcal{A}^\mu\,, \tag{14}$$

$$D^\mu \xi_R = \partial^\mu \xi_R - i g_\rho \rho^\mu \xi_R - i g_\omega \omega^\mu \xi_R + i \xi_R \mathcal{R}^\mu + i \xi_R \mathcal{A}^\mu\,, \tag{15}$$

with $\mathcal{L}^\mu$, $\mathcal{R}^\mu$ and $\mathcal{A}^\mu$ being the external gauge fields corresponding to $\mathrm{SU}(2)_L \times \mathrm{SU}(2)_R \times \mathrm{U}(1)_A$ global symmetry. We note that mesons do not carry the baryon number, so that the external gauge field corresponding to U(1) baryon number does not appear in the above covariant derivative. We also note that the covariant derivative acting on the baryon fields includes the external gauge field $\mathcal{A}^\mu$.)

By using these 1-forms, the HLS-invariant Lagrangian including the interaction terms among the nucleons and the vector mesons is given by

$$\begin{aligned}
\mathcal{L}_V = {} & a_{VNN}\left[\bar{N}_{1l}\gamma^\mu \xi_L^\dagger \hat{\alpha}_{\parallel\mu} \xi_L N_{1l} + \bar{N}_{1r}\gamma^\mu \xi_R^\dagger \hat{\alpha}_{\parallel\mu} \xi_R N_{1r}\right] \\
& + a_{VNN}\left[\bar{N}_{2l}\gamma^\mu \xi_R^\dagger \hat{\alpha}_{\parallel\mu} \xi_R N_{2l} + \bar{N}_{2r}\gamma^\mu \xi_L^\dagger \hat{\alpha}_{\parallel\mu} \xi_L N_{2r}\right] \\
& + a_{0NN}\sum_{i=1,2}\left[\bar{N}_{il}\gamma^\mu \mathrm{tr}[\hat{\alpha}_{\parallel\mu}] N_{il} + \bar{N}_{ir}\gamma^\mu \mathrm{tr}[\hat{\alpha}_{\parallel\mu}] N_{ir}\right] \\
& + \frac{{m_\rho}^2}{{g_\rho}^2}\mathrm{tr}[\hat{\alpha}_\parallel^\mu \hat{\alpha}_{\parallel\mu}] + \left(\frac{{m_\omega}^2}{8{g_\omega}^2} - \frac{{m_\rho}^2}{2{g_\rho}^2}\right)\mathrm{tr}[\hat{\alpha}_\parallel^\mu]\mathrm{tr}[\hat{\alpha}_{\parallel\mu}] - \frac{1}{8{g_\omega}^2}\mathrm{tr}[\omega^{\mu\nu}\omega_{\mu\nu}] - \frac{1}{2{g_\rho}^2}\mathrm{tr}[\rho^{\mu\nu}\rho_{\mu\nu}] \\
& + \lambda_{\omega\rho}(a_{VNN} + a_{0NN})^2 a_{VNN}^2\left[\frac{1}{2}\mathrm{tr}[\hat{\alpha}_\parallel^\mu \hat{\alpha}_{\parallel\mu}]\mathrm{tr}[\hat{\alpha}_\parallel^\nu]\mathrm{tr}[\hat{\alpha}_{\parallel\nu}] - \frac{1}{4}\left\{\mathrm{tr}[\hat{\alpha}_\parallel^\mu]\mathrm{tr}[\hat{\alpha}_{\parallel\mu}]\right\}^2\right],
\end{aligned} \tag{16}$$

where $\rho^{\mu\nu}$ and $\omega^{\mu\nu}$ are the field strengths of the ρ meson and the ω meson, given by

$$\begin{aligned}
\rho_{\mu\nu} = {} & \partial_\mu \rho_\nu - \partial_\nu \rho_\mu - i g_\rho \left[\rho_\mu\,,\, \rho_\nu\right]\,, \\
\omega_{\mu\nu} = {} & \partial_\mu \omega_\nu - \partial_\nu \omega_\mu\,.
\end{aligned} \tag{17}$$

We note that the last term in Equation (16) is a mixing term of ρ and ω mesons, as introduced in Ref. [66] to the a_0 model to reduce the slope parameter, following Ref. [37].

As we will show in Section 4.3, when we just add the effect of $a_0(980)$ meson to the PDM without this vector meson mixing term, the slope parameter becomes too large compared with the recent constraints as summarized in Ref. [72].

Finally, the baryonic Lagrangian $\mathcal{L}_N$ based on the parity doubling structure [3,5] is given by

$$\begin{aligned}\mathcal{L}_{\mathcal{N}} = &\bar{N}_1 i\gamma^\mu \mathcal{D}_\mu N_1 + \bar{N}_2 i\gamma^\mu \mathcal{D}_\mu N_2 \\ &- m_0[\bar{N}_1\gamma_5 N_2 - \bar{N}_2\gamma_5 N_1] \\ &- g_1[\bar{N}_{1l} M N_{1r} + \bar{N}_{1r} M^\dagger N_{1l}] \\ &- g_2[\bar{N}_{2r} M N_{2l} + \bar{N}_{2l} M^\dagger N_{2r}],\end{aligned} \tag{18}$$

where $N_{ir} = \frac{1+\gamma_5}{2} N_i$ ($N_{il} = \frac{1-\gamma_5}{2} N_i$) ($i = 1, 2$) is the right-handed (left-handed) component of the nucleon fields N_i, and the covariant derivatives of the nucleon fields are defined as

$$\begin{aligned}\mathcal{D}^\mu N_{1l,2r} &= (\partial^\mu - i\mathcal{L}^\mu - i\mathcal{V}^\mu + i\mathcal{A}^\mu) N_{1l,2r}\,, \\ \mathcal{D}^\mu N_{1r,2l} &= (\partial^\mu - i\mathcal{R}^\mu - i\mathcal{V}^\mu - i\mathcal{A}^\mu) N_{1r,2l}\,,\end{aligned} \tag{19}$$

where $\mathcal{V}^\mu$ is the external gauge field corresponding to the U(1) baryon number. By diagonalizing $\mathcal{L}_N$, we obtain two baryon fields N_+ and N_- corresponding to the positive parity and negative parity nucleon fields, respectively. Their masses in vacuum are obtained as [3,5]

$$m_\pm^{(\mathrm{vac})} = \frac{1}{2}\left[\sqrt{(g_1+g_2)^2\sigma_0^2 + 4m_0^2} \pm (g_1 - g_2)\sigma_0\right]. \tag{20}$$

In the present work, N_+ and N_- are identified as $N(939)$ and $N(1535)$, respectively.

2.2. Dense Nuclear Matter in PDM with Mean Field Approximation

To construct the nuclear matter from the model introduced in the previous section, we adopt the mean-field approximation following Ref. [19]. As a first step, we reduce the effect of $a_0(980)$ meson and vector meson mixing interaction to study the dense nuclear matter. The effect of $a_0(980)$ meson and vector meson mixing will be studied in Section 4.

The meson fields are then given by

$$\sigma(x) \to \sigma\,, \quad \vec{\pi}(x) \to 0\,, \quad \vec{a}_0(x) \to 0\,, \quad \eta(x) \to 0\,, \tag{21}$$

and then, the mean field for M becomes

$$\langle M \rangle = \begin{pmatrix} \sigma & 0 \\ 0 & \sigma \end{pmatrix}. \tag{22}$$

Now, the potential V_M is written in terms of the meson mean fields as

$$V_M = -\frac{\bar{\mu}_\sigma^2}{2}\sigma^2 + \frac{\lambda_4}{4}\sigma^4 - \frac{\lambda_6}{6}\sigma^6 - m_\pi^2 f_\pi \sigma. \tag{23}$$

Here, the parameters are defined as

$$\begin{aligned}\bar{\mu}_\sigma^2 &\equiv \bar{\mu}^2 + \frac{1}{2}K\,, \\ \lambda_4 &\equiv \lambda_{41} - \lambda_{42}, \\ \lambda_6 &\equiv \lambda_{61} + \lambda_{62} + \lambda_{63}.\end{aligned} \tag{24}$$

In the mean-field approximation, the vector meson fields are taken as

$$\omega_\mu(x) \to \omega\delta_{\mu 0}, \qquad \rho_\mu^i(x) \to \rho\delta_{\mu 0}\delta_{i3}, \tag{25}$$

according to the rotational symmetry and isospin symmetry. Subsequently, the Lagrangian of the vector mesons is expressed in terms of the mean fields as

$$\mathcal{L}_V = -g_{\omega NN}\sum_{\alpha j}\bar{N}_{\alpha j}\gamma^0\omega N_{\alpha j} - g_{\rho NN}\sum_{\alpha j}\bar{N}_{\alpha j}\gamma^0\frac{\tau_3}{2}\rho N_{\alpha j} + \frac{1}{2}m_\omega^2\omega^2 + \frac{1}{2}m_\rho^2\rho^2. \tag{26}$$

with

$$g_{\omega NN} = (a_{VNN} + a_{0NN})g_\omega\,, \tag{27}$$
$$g_{\rho NN} = a_{VNN}g_\rho\,. \tag{28}$$

We note that, as we stated in the beginning of this subsection, we take $\lambda_{\omega\rho} = 0$ to turn off the vector meson mixing interaction for the moment.

Then, the thermodynamic potential for the nucleons is written as

$$\Omega_N = -2\sum_{\alpha=\pm,j=\pm}\int^{k_f}\frac{d^3p}{(2\pi)^3}\left[\mu_j^* - \omega_{\alpha j}\right], \tag{29}$$

where $\alpha = \pm$ denotes the parity and $j = \pm$ the iso-spin of nucleons. μ_j^* is the effective chemical potential, given by

$$\mu_j^* \equiv (\mu_B - g_{\omega NN}\omega) + \frac{j}{2}(\mu_I - g_{\rho NN}\rho)\,, \tag{30}$$

and $\omega_{\alpha j}$ is the energy of the nucleon defined as $\omega_{\alpha j} = \sqrt{(\vec{p})^2 + (m_{\alpha j}^*)^2}$, with $\vec{p}$ and $m_{\alpha j}^*$ being the momentum and the effective mass of the nucleon. The effective mass $m_{\alpha j}^*$ is given by

$$m_{\alpha j}^* = \frac{1}{2}\left[\sqrt{(g_1+g_2)^2\sigma^2 + 4m_0^2} + \alpha(g_1 - g_2)\sigma\right]. \tag{31}$$

The entire thermodynamic potential for hadronic matter is expressed as

$$\Omega_H = \Omega_N - \frac{\bar{\mu}_\sigma^2}{2}\sigma^2 + \frac{\lambda_4}{4}\sigma^4 - \frac{\lambda_6}{6}\sigma^6 - m_\pi^2 f_\pi\sigma - \frac{1}{2}m_\omega^2\omega^2 - \frac{1}{2}m_\rho^2\rho^2 - \Omega_0\,, \tag{32}$$

where we subtracted the potential at the vacuum

$$\Omega_0 \equiv -\frac{\bar{\mu}_\sigma^2}{2}f_\pi^2 + \frac{\lambda_4}{4}f_\pi^4 - \frac{\lambda_6}{6}f_\pi^6 - m_\pi^2 f_\pi^2\,. \tag{33}$$

2.3. Nuclear Saturation Properties

Nuclear properties at the saturation density $n_0 = 0.16$ fm^{-3} are very important to be satisfied in nuclear physics. At the saturation, the energy per nucleon of the infinite symmetric nuclear matter is minimized. There are several fundamental nuclear properties at the saturation density: the binding energy B_0, the nuclear incompressibility K_0, the nuclear symmetry energy S_0, and the slope parameter L_0. In the present work, the model parameters are determined such that the saturation properties of the nuclear matter are reproduced.

We first obtain the pressure of hadronic matter P from the thermodynamic potential in Equation (86) as

$$P(\mu_B, \mu_I) = -\Omega_H(\mu_B, \mu_H; \sigma = \sigma_0, \omega = \omega_0, \rho = \rho_0)\,, \tag{34}$$

where μ_B and μ_I are the chemical potentials for the baryon number and the isospin number, and σ_0, ω_0 and ρ_0 are the solutions of the stationary conditions of Ω_H, given by

$$\frac{\partial\Omega_H}{\partial\sigma} = 0\,, \quad \frac{\partial\Omega_H}{\partial\omega} = 0\,, \quad \frac{\partial\Omega_H}{\partial\rho} = 0\,. \tag{35}$$

From the pressure P, we define the baryon number density n_B and the isospin density n_I as

$$n_B = \frac{\partial P}{\partial \mu_B}\,, \quad n_I = \frac{\partial P}{\partial \mu_I}\,. \tag{36}$$

They are related to the proton number density n_p and the neutron number density n_n as

$$n_B = n_p + n_n\,, \quad n_I = \frac{1}{2}n_p - \frac{1}{2}n_n\,. \tag{37}$$

As usual, from these densities and the pressure, we obtain the energy density ϵ via the Legendre transformation as

$$\epsilon(n_B, n_I) = -P + \mu_B n_B + \mu_I n_I\,. \tag{38}$$

It is convenient to define the energy per nucleon as

$$w(x,\delta) \equiv \frac{\epsilon(n_B, n_I)}{n_B} - m_N, \tag{39}$$

where

$$x \equiv \frac{n_B - n_0}{3n_0}\,, \quad \delta \equiv -\frac{2n_I}{n_B}\,. \tag{40}$$

At the saturation density $n_B = n_0$, the symmetric nuclear matter ($n_I = 0$) forms the most stable state with minimized energy. In other words, $w(x,\delta)$ is stationary when $(x,\delta) = (0,0)$, with $w(0,0) < 0$. Then,

$$\frac{\partial w}{\partial \delta}\Big|_0 = \frac{\partial w}{\partial n_B}\frac{\partial n_B}{\partial \delta} + \frac{\partial w}{\partial n_I}\frac{\partial n_I}{\partial \delta}\Big|_0 = -\frac{1}{2}\mu_I\Big|_0 = 0, \tag{41}$$

$$\frac{\partial w}{\partial x}\Big|_0 = \frac{3P}{n_0}\Big|_0 = 0\,, \tag{42}$$

where $\Big|_0$ means that the derivatives are evaluated at $(x,\delta) = (0,0)$. These imply that the pressure P and isospin chemical potential μ_I are zero at the saturation density. The binding energy B_0 is obtained as

$$B_0 = -w(0,0) = -\frac{\epsilon}{n_B}\Big|_0 + m_N = -\mu_B\Big|_0 + m_N\,. \tag{43}$$

In this review, we take $B_0 = -16\,\mathrm{MeV}$ as an input.

Expanding $w(x,\delta)$ around the stationary point $(x,\delta) = (0,0)$, we obtain

$$\begin{aligned} w(x,\delta) &= w(0,0) + \frac{1}{2}\frac{\partial^2 w}{\partial x^2}\Big|_0 x^2 + \frac{1}{2}\frac{\partial^2 w}{\partial \delta^2}\Big|_0 \delta^2 + \frac{1}{2}\frac{\partial^3 w}{\partial x \partial \delta^2}\Big|_0 x\delta^2 + O(x^3) \\ &\equiv -B_0 + \frac{1}{2}K_0 x^2 + (S_0 + L_0 x)\delta^2 + O(x^3)\,, \end{aligned} \tag{44}$$

where K_0, S_0, and L_0 are called as the incompressibility, the symmetry energy, and the slope parameter at the saturation density, respectively.

The incompressibility K_0 represents the curvature of $w(x,\delta)$ in the direction of the baryon number density. It corresponds to the rate of increase of the baryon chemical potential μ_B with respect to n_B around the saturation density. K_0 is calculated as

$$K_0 \equiv \frac{\partial^2 w}{\partial x^2}\Big|_0 = 9n_0^2\frac{\partial^2}{\partial n_B^2}\left(\frac{\epsilon}{n_B}\right)\Big|_0 = 9n_0\frac{\partial \mu_B}{\partial n_B}\Big|_0. \tag{45}$$

We note that K_0 corresponds to the hardness of the (symmetric) matter around the saturation density; the larger K_0 corresponds to the larger pressure at high baryon density. Thus, it is called the incompressibility of nuclear matter because a larger K_0 corresponds to a matter that is more resistant to compression. The generally accepted values are $K_0 = 240 \pm 40$ (see recent review [73] for detailed discussion and summary of the values of K_0). In this review, the results are mainly computed with K_0 = 215, 240 MeV for comparison.

The symmetry energy S_0 is defined to be the slope of $w(x, \delta)$ in the isospin density direction around n_0 as

$$S_0 \equiv \frac{1}{2}\frac{\partial^2 w}{\partial \delta^2}\Big|_0 = \frac{n_0^2}{8}\frac{\partial^2}{\partial n_I^2}\left(\frac{\epsilon}{n_B}\right)\Big|_0 = \frac{n_0}{8}\frac{\partial \mu_I}{\partial n_I}\Big|_0. \tag{46}$$

The symmetry energy is the energy that arises from the asymmetry of the matter. If we ignore the $O(x^3)$ contribution in Equation (44), the symmetry energy at the saturation density S_0 can be approximated by

$$S_0 \approx w(0,1) - w(0,0), \tag{47}$$

which is the energy difference between pure neutron matter and symmetric matter. Then, the term $S_0\delta^2$ can be seen as the energy arises from the difference of n_p and n_n (the asymmetry of the matter) around the saturation density. For later convenience, we define the symmetry energy at arbitrary baryon density n_B as

$$S(n_B) \equiv \frac{1}{2}\frac{\partial^2 w(x,\delta)}{\partial \delta^2}\bigg|_{\delta=0}. \tag{48}$$

This $S(n_B)$ approximately corresponds to the energy difference between pure neutron matter and symmetric matter at n_B:

$$S(n_B) \approx w(x,1) - w(x,0). \tag{49}$$

The value of S_0 is well-studied with little ambiguity. In this review, S_0 is taken to be 31 MeV.

Finally, the slope parameter L_0 is given by

$$L_0 \equiv \frac{1}{2}\frac{\partial^3 w}{\partial x \partial \delta^2}\Big|_0 = \frac{\partial S(n_B)}{\partial x}\Big|_0 = 3S_0 + \frac{3n_0^2}{8}\frac{\partial^2 \mu_I}{\partial n_B n_I}\Big|_0. \tag{50}$$

The slope parameter approximates the slope of the symmetry energy in the direction of baryon number density around the saturation density. The larger L_0 results in the larger symmetry energy $S(n_B)$ at higher density. Due to the experimental difficulties, the value of L_0 possesses large uncertainty and has been discussed for many years. The recent accepted values are $L_0 = 57.7 \pm 19$ MeV, as summarized in Ref. [72].

2.4. Determination of Model Parameters

In the present model, the model parameters are fitted to reproduce the nuclear saturation properties, as well as physical masses and the decay constant in vacuum. Under the mean field approximation in Section 2.2, there are seven parameters to be determined for a given value of the chiral invariant mass m_0:

$$g_1\,,\ g_2\,,\ \bar{\mu}_\sigma^2\,,\ \lambda_4\,,\ \lambda_6\,,\ g_{\omega NN}\,,\ g_{\rho NN}\,. \tag{51}$$

The vacuum expectation value of σ is taken to be $\sigma_0 = f_\pi$ with the pion decay constant $f_\pi = 93$ MeV. The Yukawa coupling constants g_1 and g_2 are determined by fitting them to the nucleon masses in vacuum given in Equation (20), with $m_+ = m_N = 939$ MeV and $m_- = m_{N^*} = 1535$ MeV for fixed value of the chiral invariant mass m_0. The values of

$\bar{\mu}_\sigma^2$, λ_4, λ_6, $g_{\omega NN}$, and $g_{\rho NN}$ are determined by the saturation properties shown in Table 1 together with the stationary condition of the potential in vacuum given by

$$\bar{\mu}_\sigma^2 f_\pi - \lambda_4 f_\pi^3 + \lambda_6 f_\pi^5 + m_\pi^2 f_\pi = 0\,. \tag{52}$$

For the meson masses, we use the values listed in Table 2. We should note that there is a relatively large uncertainty in the incompressibility, so we use $K_0 = 215$ and 240 MeV as inputs for studying the dependence. The determined values of the parameters for a fixed value of m_0 are summarized in Table 3.

Table 1. Saturation properties that are used to determine the model parameters: saturation density n_0, binding energy B_0, incompressibility K_0, and symmetry energy S_0.

n_0 [fm^{-3}]	B_0 [MeV]	K_0 [MeV]	S_0 [MeV]
0.16	16	215, 240	31

Table 2. Values of meson masses and pion decay constant in the vacuum in unit of MeV.

m_π	m_ω	m_ρ	f_π
140	783	776	93

Table 3. Values of g_1, g_2, $\bar{\mu}_\sigma^2$, λ_4, λ_6, $g_{\omega NN}$, $g_{\rho NN}$ for m_0 = 600–900 MeV, $K_0 = 215, 240$ MeV.

	m_0 [MeV]	600	700	800	900
$K_0 = 215$ MeV	g_1	8.427	7.762	6.941	5.921
	g_2	14.836	14.171	13.349	12.329
	$\bar{\mu}_\sigma^2/f_\pi^2$	23.377	20.979	13.346	2.502
	λ_4	42.368	38.92	26.128	6.673
	$\lambda_6 f_\pi^2$	16.79	15.739	10.58	1.969
	$g_{\omega NN}$	8.902	7.055	5.471	3.389
	$g_{\rho NN}$	7.896	8.16	8.314	8.442
$K_0 = 240$ MeV	g_1	8.427	7.762	6.941	5.921
	g_2	14.836	14.171	13.349	12.329
	$\bar{\mu}_\sigma^2/f_\pi^2$	21.821	18.842	11.692	1.537
	λ_4	39.367	34.583	22.577	4.388
	$\lambda_6 f_\pi^2$	15.344	13.54	8.683	0.649
	$g_{\omega NN}$	9.132	7.305	5.66	3.522
	$g_{\rho NN}$	7.854	8.13	8.298	8.436

The slope parameter L_0 is computed as an output, and the resultant values are shown in Table 4. We note that the computed L_0 is slightly larger than the recently accepted values $L_0 = 57.7 \pm 19$ MeV, as summarized in Ref. [72]. We also observe that the value of incompressibility has little effect on L_0, even with a large $K_0 = 260$ MeV.

Table 4. Slope parameter L_0 computed as a output from the model with $K_0 = 215, 240, 260$ MeV. $S_0 = 31$ MeV.

	m_0 [MeV]	600	700	800	900
$K_0 = 215$ MeV	L_0 [MeV]	85.91	82.87	81.32	80.15
$K_0 = 240$ MeV	L_0 [MeV]	86.25	83.04	81.33	80.08
$K_0 = 260$ MeV	L_0 [MeV]	86.45	83.14	81.33	80.03

The dependence of L_0 on S_0 is compared in Table 5. We observe that the value of S_0 have a relatively large impact on the value of L_0.

Table 5. Slope parameter L_0 with $S_0 = 24, 31, 36$ MeV. $K_0 = 215$ MeV.

	m_0 [MeV]	600	700	800	900
$S_0 = 24$ MeV	L_0 [MeV]	64.91	61.87	60.32	59.15
$S_0 = 31$ MeV	L_0 [MeV]	85.91	82.87	81.32	80.15
$S_0 = 36$ MeV	L_0 [MeV]	100.91	97.87	96.32	95.15

3. Finite Nuclei

In the previous section, we observed that the parity doublet model reproduces reasonably the nuclear matter saturation properties with the chiral invariant nucleon mass m_0 in the range of 600–900 MeV. In this section, we study the properties of nuclei in self-consistent relativistic mean field theory to see if the parity doublet model can explain some nuclear properties, and to find out the value of the chiral invariant mass preferred by nuclear structures. As a first step, we use the PDM without the a_0 meson, focusing on the properties of stable nuclei. Nuclear properties in the PDM with the a_0 meson is being studied and the results will be reported elsewhere.

Before we investigate the properties of nuclei using the PDM, we first describe how one obtains the nuclear energy density functional based on the relativistic mean field theory and the corresponding equation of motion for nucleons and mesons. We also discuss, in brief, how to solve the equation of motion, especially for exotic nuclei in which the continuum effect is important. For this, we closely follow the description in Ref. [68], where a Walecka-type model was adopted. The Relativistic Continuum Hartree–Bogoliubov (RCHB) theory [68] is an extension of the relativistic mean field theory in a self-consistent way with both bound and (discretized) continuum states.

The starting Lagrangian is given by

$$\begin{aligned}\mathcal{L} = \bar{\psi}[i\partial\!\!\!/ - M - g_\sigma\sigma - g_\omega\omega\!\!\!/ - g_\rho\rho\!\!\!/ - eA\!\!\!/\frac{1-\tau_3}{2}]\psi + \frac{1}{2}\partial^\mu\sigma\partial_\mu\sigma - U(\sigma) \\ -\Omega^{\mu\nu}\Omega_{\mu\nu} + U_\omega(\omega_\mu) - \frac{1}{4}\vec{R}^{\mu\nu}\cdot\vec{R}_{\mu\nu} + U_\rho(\vec{\rho}_\mu) - \frac{1}{4}F_{\mu\nu}F_{\mu\nu}\,,\end{aligned} \tag{53}$$

where $\Omega^{\mu\nu}$, $\vec{R}^{\mu\nu}$ and $F_{\mu\nu}$ are the field strength tensors of the ω meson, ρ meson and electromagnetic field, respectively and

$$\begin{aligned}U(\sigma) &= \frac{1}{2}m_\sigma^2\sigma^2 + \frac{1}{3}g_2\sigma^3 + \frac{1}{4}g_3\sigma^4\,, \\ U_\omega(\omega_\mu) &= \frac{1}{2}m_\omega^2\omega_\mu\omega^\mu + \frac{1}{4}c_3(\omega_\mu\omega^\mu)^2\,, \\ U_\rho(\vec{\rho}_\mu) &= \frac{1}{2}m_\rho^2\vec{\rho}_\mu\vec{\rho}^\mu + \frac{1}{4}d_3(\vec{\rho}_\mu\vec{\rho}^\mu)^2\,,\ \rho = \vec{\rho}\cdot\vec{\tau}\,.\end{aligned} \tag{54}$$

We refer to Table 2 in Ref. [68] for the value of the masses and coupling constants in the above Lagrangian that were determined by studying the properties of nuclear matter and a few doubly magic nuclei with no-sea and mean-field approximations. After taking the mean field approximation on the above Lagrangian and performing the Legendre transformation, we obtain the corresponding mean field Hamiltonian $\mathcal{H}_{\rm RMF}$ and the energy density functional $E_{\rm RMF} = \langle\Phi|\mathcal{H}_{\rm RMF}|\Phi\rangle$. Here, $|\Phi\rangle$ is the ground state of a nucleus with the mass number A, $|\Phi\rangle = \prod_{a=1}^{A} c_a^\dagger|0\rangle$, and $c_a^\dagger$ is the creation operator of the nucleon field, $\psi(x) = \sum_a \psi_a(x)c_a$. Then, the expectation value of the Hamiltonian with the mean field approximation reads

$$
\begin{aligned}
E_{\mathrm{RMF}}(\rho,\phi) &= \langle\Phi|\mathcal{H}_{\mathrm{RMF}}|\Phi\rangle \\
&= \int d^3x \mathrm{Tr}[\beta(\vec{\gamma}\cdot\vec{p}+M+g_\sigma\sigma+g_\omega\beta\omega_0+g_\rho\beta\rho_0^3\tau_3+ e\not{A}\frac{1-\tau_3}{2})\rho] \\
&\quad + \int d^3x[-\frac{1}{2}\partial^i\sigma\partial_i\sigma+U_\sigma(\sigma)+\frac{1}{4}\Omega^{ij}\Omega_{ij}-U_\omega(\omega_0)+\frac{1}{4}\vec{R}^{ij}\cdot\vec{R}_{ij}-U_\rho(\rho_0^3) \\
&\qquad -\frac{1}{4}F^{0j}F_{0j}]\,,
\end{aligned} \tag{55}
$$

where ρ is the density matrix, ϕ represents bosonic fields, and $\gamma^\mu = (\beta, \beta\vec{\alpha})$. Here, we assumed that the mean field is time-independent. Also, we have applied the fact that the spatial components of the vector fields are zero in a system with the time reversal symmetry. By performing variations on E_{RMF} with respect to ρ and ϕ, we obtain the equations for the nucleon and bosons [68].

$$
h_D\psi_i(\vec{x}) = \epsilon_i\psi_i(\vec{x})\,, \tag{56}
$$

where the Dirac Hamiltonian h_D is given by

$$
h_D = \vec{\alpha}\cdot\vec{p}+\beta[M+S(\vec{x})]+V(\vec{x}) \tag{57}
$$

with the scalar $S(\vec{x})$ and vector $V(\vec{x})$ potentials given by

$$
\begin{aligned}
S(\vec{x}) &= g_\sigma\sigma(\vec{x})\,, \\
V(\vec{x}) &= g_\omega\omega_0(\vec{x})+g_\rho\tau_3\rho_0^3(\vec{x})+\frac{1}{2}e(1-\tau_3)A_0(\vec{x})\,.
\end{aligned}
$$

In general, the equations of motion for the nucleon moving in the mean field potentials are solved by using the harmonic oscillator basis. However, for exotic nuclei, whose density profile can have a long tail, it is preferable to solve the equations in coordinate space and adopt a basis which can treat the asymptotic behavior of the nucleon wave function. In Ref. [68], the Woods–Saxon basis was used to solve the equations of motion for the nucleon.

Similarly, by doing variations on E_{RMF} with respect to ϕ, we obtain the equations for the bosons [68],

$$
\begin{aligned}
-\vec{\nabla}^2\sigma+U'_\sigma(\sigma) &= -g_\rho\rho_3\,, \\
-\vec{\nabla}^2\omega_0+U'_\omega(\omega_0) &= g_\omega\rho_\omega\,, \\
-\vec{\nabla}^2\rho_0^3+U'_\rho(\rho_0^3) &= g_\rho\rho_3\,, \\
-\vec{\nabla}^2A_0 &= e\rho_c\,.
\end{aligned} \tag{58}
$$

where

$$
\begin{aligned}
\rho_s &= \mathrm{Tr}[\beta\rho]\,, \\
\rho_\omega &= \mathrm{Tr}[\rho]\,, \\
\rho_3 &= \mathrm{Tr}[\tau_3\rho]\,, \\
\rho_c &= \mathrm{Tr}[(1-\tau_3)\rho]\,.
\end{aligned} \tag{59}
$$

Using Equation (58) in Equation (55), one can obtain the total energy of the system as

$$
\begin{aligned}
E &= \int d^3x \mathrm{Tr}[\beta(\vec{\gamma}\cdot\vec{p}+M)\rho+\frac{1}{2}(g_\sigma\beta\sigma+g_\omega\omega_0+g_\rho\rho_0^3\tau_3+A_0\frac{1-\tau_3}{2})\rho] \\
&\quad + \int d^3x[U_\sigma(\sigma)-U_\omega(\omega_0)-U_\rho(\rho_0^3)-\frac{1}{2}(\sigma U'_\sigma(\sigma)-\omega_0U'_\omega(\omega_0)-\rho_0^3U'_\rho(\rho_0^3))]\,.
\end{aligned} \tag{60}
$$

Now, we move onto the PDM without the a_0 meson. To pin down the value of m_0, we study the properties of nuclei using the parity doublet model without the a_0 meson in the framework of a self-consistent relativistic mean field theory.

Using the Lagrangian of the parity doublet model without the a_0 meson in Equation (1), we obtain the equations of motion (EoM) for the stationary mean fields σ, ω_0, ρ_0^3 and A_0 [67],

$$\begin{aligned}
\left(-\vec{\nabla}^2 + m_\sigma^2\right)\langle\sigma(\vec{x})\rangle &= -\bar{N}(\vec{x})N(\vec{x})\left.\frac{\partial\, m_N^*(\sigma)}{\partial\sigma}\right|_{\sigma=\langle\sigma(\vec{x})\rangle} \\
&\quad + \left(-3f_\pi\lambda_4 + 10f_\pi^3\lambda_6\right)\langle\sigma(\vec{x})\rangle^2 \\
&\quad + \left(-\lambda_4 + 10f_\pi^2\lambda_6\right)\langle\sigma(\vec{x})\rangle^3 \\
&\quad + 5f_\pi\lambda_6\langle\sigma(\vec{x})\rangle^4 + \lambda_6\langle\sigma(\vec{x})\rangle^5\,, \qquad (61)\\
\left(-\vec{\nabla}^2 + m_\omega^2\right)\langle\omega_0(\vec{x})\rangle &= g_{\omega NN}N^\dagger(\vec{x})N(\vec{x})\,, \qquad (62)\\
\left(-\vec{\nabla}^2 + m_\rho^2\right)\langle\rho_0^3(\vec{x})\rangle &= g_{\rho NN}N^\dagger(\vec{x})\frac{\tau^3}{2}N(\vec{x})\,, \qquad (63)\\
-\vec{\nabla}^2\langle A_0(\vec{x})\rangle &= eN^\dagger(\vec{x})\frac{1-\tau_3}{2}N(\vec{x})\,. \qquad (64)
\end{aligned}$$

Note here that we take the shift $\sigma \to f_\pi + \sigma$, since the scalar field in the parity doublet model is a chiral partner of the pion field, whose vacuum expectation value in free space is f_π, while that of the widely used scalar field in nuclear structure studies is zero in free space. Since we are interested in finite nuclei, we will not consider the EoM for the parity partner of the nucleon, $N^*(1535)$, which does not form its Fermi sea near the saturation density. In addition, since our primary goal here is to see if the parity doublet model can explain some basic nuclear properties, such as the binding energy with a reasonable value of the chiral invariant mass, we will not consider pairing correlations, which are essential for odd–even staggering in nuclear properties. For instance, according to the semi-empirical mass formula, the contribution from the pairing term to the binding energy per nucleon of ^{58}Ni is only about 0.03 MeV.

The EoM for the nucleon is given by

$$\left[\vec{\alpha}\cdot\vec{p} + \beta\, m_N^*(\langle\sigma(\vec{x})\rangle) + V(\vec{x})\right]N_i(\vec{x}) = \epsilon_i N_i(\vec{x})\,, \qquad (65)$$

where N_i is the single-particle wave function, and

$$V(\vec{x}) = g_{\omega NN}\langle\omega_0(\vec{x})\rangle + g_{\rho NN}\langle\rho_0^3(\vec{x})\rangle\frac{\tau^3}{2} + e\frac{(1-\tau_3)}{2}\langle A_0(\vec{x})\rangle\,. \qquad (66)$$

With assuming the spherical shape of the nucleus, we can solve Equations (61)–(65) simultaneously to obtain the energy

$$E = \int d^3x\, \mathcal{H}(\vec{x})\,. \qquad (67)$$

After subtracting out the vacuum contribution, we write the Hamiltonian density $\mathcal{H}(\vec{x})$ in the mean field approximation as

$$\begin{aligned}
\mathcal{H} &= \bar{N}\left(-i\gamma^i\partial_i + m_N^*\right)N + g_{\omega NN}\langle\omega_0\rangle N^\dagger N + g_{\rho NN}\langle\rho_0^3\rangle N^\dagger\frac{\tau^3}{2}N + e\langle A_0\rangle N^\dagger\frac{1-\tau_3}{2}N \\
&\quad -\frac{1}{2}\partial^i\langle\sigma\rangle\partial_i\langle\sigma\rangle + \frac{1}{2}\partial^i\langle\omega_0\rangle\partial_i\langle\omega_0\rangle + \frac{1}{2}\partial^i\langle\rho_0^3\rangle\partial_i\langle\rho_0^3\rangle + \frac{1}{2}\partial^i\langle A_0\rangle\partial_i\langle A_0\rangle \\
&\quad -\frac{\bar{\mu}_\sigma^2}{2}\left[(f_\pi+\langle\sigma\rangle)^2 - f_\pi^2\right] + \frac{\lambda_4}{4}\left[(f_\pi+\langle\sigma\rangle)^4 - f_\pi^4\right] - \frac{\lambda_6}{6}\left[(f_\pi+\langle\sigma\rangle)^6 - f_\pi^6\right] - m_\pi^2 f_\pi\langle\sigma\rangle \\
&\quad -\frac{1}{2}m_\omega^2\langle\omega_0\rangle^2 - \frac{1}{2}m_\rho^2\langle\rho_0^3\rangle^2\,. \qquad (68)
\end{aligned}$$

Then, the binding energy (BE) per nucleon is given by

$$\mathrm{BE}/A = -\frac{E}{A} + m_N\,. \tag{69}$$

To put an additional constraint on the value of the chiral invariant mass, using the model parameters summarized in Table 3, we calculate the binding energies per nucleon and charge radii of selected nuclei: ^{16}O, ^{40}Ca, ^{48}Ca, ^{58}Ni, ^{70}Ge, ^{82}Se, ^{92}Mo, ^{112}Sn, ^{126}Sn, ^{138}Ba, ^{154}Sm, ^{170}Er, ^{182}W, ^{202}Pb and ^{208}Pb [67]. Before we compare our results for the binding energies and charge radii with the experiments, we show the nucleon density profile, mean-field value and effective nucleon mass in a nucleus with different values of the chiral invariant mass to visualize how the chiral invariant mass affects them. We first plot the nucleon density profile in ^{112}Sn and ^{126}Sn for different values of the chiral invariant mass in Figure 1. It is interesting to see that ^{112}Sn has a depleted central density and, therefore, can be a candidate of bubble nuclei, which was also observed in the previous studies based on relativistic mean field models; for example, see Ref. [74].

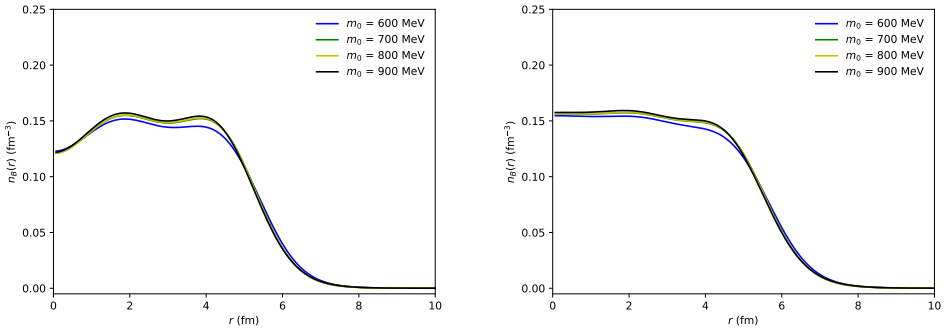

Figure 1. Nucleon density profile in ^{112}Sn (**left**) and ^{126}Sn (**right**) calculated with $K_0 = 215$ MeV.

In Figure 2, we present the value of $\langle\sigma\rangle$ and $\langle\omega_0\rangle$ in ^{112}Sn and ^{126}Sn for different values of the chiral invariant mass. As expected, the value of $\langle\sigma\rangle$ decreases and $\langle\omega_0\rangle$ increases as $r \to 0$, from zero density to the saturation density.

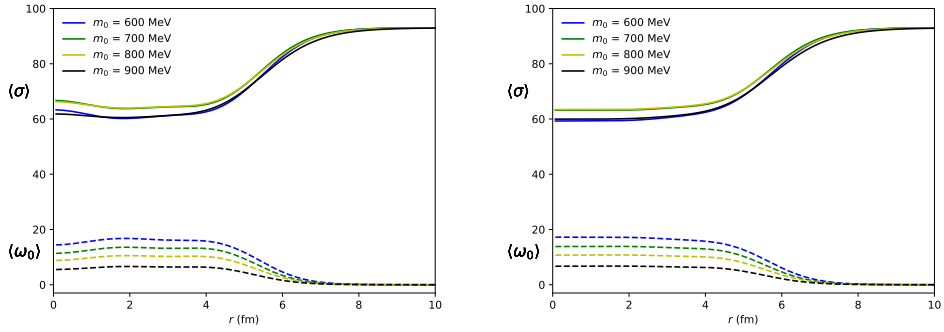

Figure 2. $\langle\sigma\rangle$ and $\langle\omega_0\rangle$ in ^{112}Sn (**left**) and ^{126}Sn (**right**) with $K_0 = 215$ MeV.

The effective neutron and proton masses in ^{112}Sn and ^{126}Sn are shown in Figure 3, where the effective mass is defined as the energy of the nucleon at rest:

$$m_n^{(\mathrm{eff})} = m_n^* + g_{\omega NN}\langle\omega_0\rangle - \frac{g_{\rho NN}}{2}\langle\rho_0\rangle\,,$$
$$m_p^{(\mathrm{eff})} = m_p^* + g_{\omega NN}\langle\omega_0\rangle + \frac{g_{\rho NN}}{2}\langle\rho_0\rangle\,.$$

As observed in Ref. [67], the neutron–proton mass difference becomes larger in a nucleus with larger isospin asymmetry.

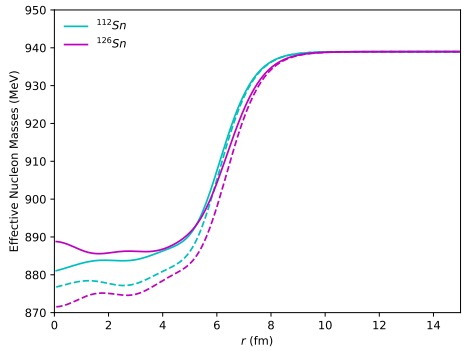

Figure 3. Neutron and proton effective masses in ^{112}Sn and ^{126}Sn with $K_0 = 215$ MeV. Here, solid (dashed) lines are for the neutron (proton).

Now, as in Ref. [67], we compare our results with experiments to check which value of the chiral invariant mass reproduces the experimental results well. In Tables 6 and 7, we present the binding energies per nucleon and the charge radii as well as the root-mean-square deviation (RMSD) with $m_0 = 600, 700, 800, 900$ MeV for selected nuclei: ^{16}O, ^{40}Ca, ^{48}Ca, ^{58}Ni, ^{70}Ge, ^{82}Se, ^{92}Mo, ^{112}Sn, ^{126}Sn, ^{138}Ba, ^{154}Sm, ^{170}Er, ^{182}W, ^{202}Pb, and ^{208}Pb [67]. It can be seen from Tables 6 and 7 that the case with $m_0 = 700$ MeV has the smallest RMS deviation both in the binding energies and charge radii. Therefore, as concluded in Ref. [67], $m_0 = 700$ MeV is preferred by the nuclear properties of selected isotopes.

Table 6. Binding energy per nucleon and the charge radius (R_C) with the parameter set in Table 3 for $K = 215$ MeV. The table is taken from Ref. [67].

m_0 (MeV)		600	700	800	900	Exp.
BE/A (MeV)	^{16}O	7.489	7.781	7.298	5.698	7.976
	^{40}Ca	8.063	8.301	7.942	6.693	8.551
	^{48}Ca	7.978	8.134	7.757	6.541	8.667
	^{58}Ni	7.685	7.841	7.473	6.308	8.732
	^{70}Ge	8.044	8.239	7.932	6.866	8.722
	^{82}Se	8.066	8.219	7.910	6.881	8.693
	^{92}Mo	7.993	8.123	7.822	6.828	8.658
	^{112}Sn	7.911	8.050	7.774	6.844	8.514
	^{126}Sn	7.980	8.070	7.802	6.909	8.443
	^{138}Ba	7.920	8.028	7.764	6.890	8.393
	^{154}Sm	7.821	7.958	7.724	6.894	8.227
	^{170}Er	7.733	7.837	7.618	6.830	8.112
	^{182}W	7.616	7.707	7.494	6.726	8.018
	^{202}Pb	7.468	7.535	7.310	6.549	7.882
	^{208}Pb	7.496	7.552	7.321	6.558	7.867
RMS deviation		0.573	0.438	0.727	1.734	–
R_C (fm)	^{16}O	2.845	2.763	2.772	2.796	2.699
	^{40}Ca	3.546	3.469	3.473	3.479	3.478
	^{48}Ca	3.585	3.521	3.525	3.527	3.478
	^{58}Ni	3.912	3.848	3.856	3.863	3.776
	^{70}Ge	4.085	4.013	4.013	4.008	4.041
	^{82}Se	4.209	4.145	4.144	4.135	4.140
	^{92}Mo	4.401	4.339	4.344	4.344	4.315
	^{112}Sn	4.671	4.608	4.609	4.602	4.594
	^{126}Sn	4.754	4.697	4.698	4.688	4.685
	^{138}Ba	4.920	4.862	4.861	4.849	4.838
	^{154}Sm	5.111	5.045	5.039	5.022	5.105
	^{170}Er	5.242	5.178	5.175	5.160	5.279
	^{182}W	5.364	5.301	5.298	5.286	5.356
	^{202}Pb	5.549	5.493	5.493	5.481	5.471
	^{208}Pb	5.584	5.531	5.532	5.519	5.501
RMS deviation		0.082	0.046	0.049	0.056	–

Table 7. Binding energy per nucleon and the charge radius (R_C) with the parameter set in Table 3 for $K = 240$ MeV. The table is taken from Ref. [67].

m_0 (MeV)		600	700	800	900	Exp.
BE/A (MeV)	^{16}O	7.087	7.280	6.792	5.093	7.976
	^{40}Ca	7.736	7.906	7.538	6.191	8.551
	^{48}Ca	7.676	7.768	7.378	6.061	8.667
	^{58}Ni	7.391	7.486	7.108	5.849	8.732
	^{70}Ge	7.761	7.900	7.584	6.429	8.722
	^{82}Se	7.799	7.899	7.580	6.462	8.693
	^{92}Mo	7.741	7.821	7.507	6.424	8.658
	^{112}Sn	7.668	7.760	7.474	6.460	8.514
	^{126}Sn	7.757	7.801	7.516	6.536	8.443
	^{138}Ba	7.695	7.758	7.482	6.526	8.393
	^{154}Sm	7.596	7.691	7.447	6.540	8.227
	^{170}Er	7.526	7.587	7.354	6.484	8.112
	^{182}W	7.418	7.466	7.237	6.387	8.018
	^{202}Pb	7.277	7.303	7.062	6.221	7.882
	^{208}Pb	7.306	7.322	7.075	6.232	7.867
RMS deviation		0.827	0.737	1.047	2.147	–
R_C (fm)	^{16}O	2.877	2.792	2.790	2.803	2.699
	^{40}Ca	3.572	3.491	3.485	3.479	3.478
	^{48}Ca	3.605	3.537	3.532	3.522	3.478
	^{58}Ni	3.932	3.863	3.861	3.855	3.776
	^{70}Ge	4.104	4.028	4.018	4.001	4.041
	^{82}Se	4.223	4.154	4.145	4.125	4.140
	^{92}Mo	4.418	4.351	4.347	4.335	4.315
	^{112}Sn	4.684	4.616	4.608	4.591	4.594
	^{126}Sn	4.764	4.703	4.695	4.675	4.685
	^{138}Ba	4.928	4.865	4.856	4.834	4.838
	^{154}Sm	5.117	5.045	5.031	5.004	5.105
	^{170}Er	5.250	5.181	5.169	5.144	5.279
	^{182}W	5.374	5.305	5.294	5.270	5.356
	^{202}Pb	5.555	5.493	5.485	5.462	5.471
	^{208}Pb	5.588	5.529	5.521	5.499	5.501
RMS deviation		0.097	0.052	0.053	0.062	–

With $m_0 = 700$ MeV, we try to improve our results of nuclear properties. For this, we use the following nuclear matter properties as inputs,

$$\begin{aligned} &\frac{E}{A} - m_N = -16.3 \text{ MeV}, \quad n_0 = 0.16 \text{ fm}^{-3}, \\ &K_0 = 215 \text{ MeV}, \qquad S_0 = 30 \text{ MeV}, \end{aligned} \tag{70}$$

and determine the model parameters again given in Table 8 [67]. With the new parameter set in Table 8, we calculate the properties of selected nuclei and compare our results with experiments and the ones obtained in RCHB with PC-PK1 [75,76] in Table 9. As in Table 9, our results are in quantitative agreement with experiments. As stated in Ref. [67], pairing correlations are not included in our current results, which will be improved in our future publications.

Table 8. Parameter set with the inputs in Equation (70). All the parameters are dimensionless except m_σ.

g_1	g_2	$g_{\omega NN}$	$g_{\rho NN}$	$\bar{\mu}_\sigma^2/f_\pi^2$	λ_4	$\lambda_6 f_\pi^2$	m_σ [MeV]
7.762	14.171	7.036	3.958	21.135	39.332	15.996	382.140

Table 9. Binding energy per nucleon and the charge radius (R_C) with the parameters in Table 8.

	BE/A [MeV]			R_C [fm]		
	PDM	**RCHB**	**Exp.**	**PDM**	**RCHB**	**Exp.**
^{16}O	8.040	7.956	7.976	2.757	2.768	2.699
^{40}Ca	8.574	8.577	8.551	3.464	3.481	3.478
^{48}Ca	8.419	8.654	8.667	3.517	3.494	3.478
^{58}Ni	8.118	8.691	8.732	3.843	3.737	3.776
^{70}Ge	8.521	8.650	8.722	4.010	4.001	4.041
^{82}Se	8.513	8.664	8.693	4.142	4.125	4.140
^{92}Mo	8.408	8.662	8.658	4.335	4.310	4.315
^{112}Sn	8.339	8.489	8.514	4.605	4.582	4.594
^{126}Sn	8.372	8.447	8.443	4.695	4.683	4.685
^{138}Ba	8.329	8.406	8.393	4.860	4.848	4.838
^{154}Sm	8.263	8.149	8.227	5.042	5.062	5.105
^{170}Er	8.140	8.000	8.112	5.176	5.224	5.279
^{182}W	8.007	7.927	8.018	5.299	5.342	5.356
^{202}Pb	7.837	7.869	7.882	5.491	5.490	5.471
^{208}Pb	7.860	7.875	7.867	5.529	5.518	5.501
RMS deviation	0.204	0.05	–	0.045	0.031	–

4. Effect of a_0 Meson to Nuclear Matter

In the previous sections, we omitted the effect of the a_0 meson when we studied nuclear matter and finite nuclei. However, the isovector scalar meson may play an important role in the asymmetric matter, such as neutron star matter and neutron-rich nuclei. In this section, we study the effect of the a_0 meson on nuclear properties such as symmetry energy and slope parameter. As we will see, the a_0 meson stiffens the matter strongly and causing a large slope parameter L_0. We include also the vector meson mixing interaction to effectively reduce the slope parameter and study the effect of it.

4.1. Dense Nuclear Matter with $a_0(980)$

To construct the nuclear matter with $a_0(980)$, we adopt the mean-field approximation by taking

$$\sigma(x) \to \sigma, \qquad \pi(x) \to 0, \qquad a_0^i(x) \to a\,\delta_{i3}, \qquad \eta(x) \to 0. \tag{71}$$

Then, the mean field for M becomes

$$\langle M \rangle = \begin{pmatrix} \sigma - a & 0 \\ 0 & \sigma + a \end{pmatrix}. \tag{72}$$

Now, the potential V_M is written in terms of the meson mean fields as

$$\begin{aligned} V_M = &-\frac{\bar{\mu}_\sigma^2}{2}\sigma^2 - \frac{\bar{\mu}_a^2}{2}a^2 + \frac{\lambda_4}{4}(\sigma^4 + a^4) + \frac{\gamma_4}{2}\sigma^2 a^2 \\ &- \frac{\lambda_6}{6}(\sigma^6 + 15\sigma^2 a^4 + 15\sigma^4 a^2 + a^6) + \lambda_6^{'}(\sigma^2 a^4 + \sigma^4 a^2) \\ &- m_\pi^2 f_\pi \sigma\,, \end{aligned} \tag{73}$$

where the parameters are defined as

$$\begin{aligned} \bar{\mu}_\sigma^2 &\equiv \bar{\mu}^2 + \frac{1}{2}K\,, \\ \bar{\mu}_a^2 &\equiv \bar{\mu}^2 - \frac{1}{2}K = \bar{\mu}_\sigma^2 - K\,, \\ \lambda_4 &\equiv \lambda_{41} - \lambda_{42}\,, \\ \gamma_4 &\equiv 3\lambda_{41} - \lambda_{42}\,, \\ \lambda_6 &\equiv \lambda_{61} + \lambda_{62} + \lambda_{63}\,, \\ \lambda_6^{'} &\equiv \frac{4}{3}\lambda_{62} + 2\lambda_{63}\,. \end{aligned} \tag{74}$$

In the present model, λ_6' is taken as a free parameter to examine the effect of λ_{62} and λ_{63} interactions, which are of sub-leading order in the large N_c expansion. Given that the λ_6' term is suppressed by $1/N_c$ compared to the λ_6 term in the large N_c expansion, we assume $|\lambda_6'| \lesssim |\lambda_6|$ holds. Consequently, we consider $\lambda_6' = 0, \pm\lambda_6$ to assess the impact of the sub-leading order six-point interactions on the symmetry energy. By default, we first set $\lambda_6' = 0$. In the end of Sections 4.3 and 4.4, we investigate the impact of λ_6' on the results by comparing the cases with $\lambda_6' = 0, \pm\lambda_6$.

In the mean-field approximation, the vector meson fields are taken as

$$\omega_\mu(x) \to \omega\delta_{\mu 0}, \qquad \rho_\mu^i(x) \to \rho\delta_{\mu 0}\delta_{i3}, \tag{75}$$

according to the rotational symmetry and isospin symmetry. Subsequently, the Lagrangian of the vector mesons is expressed in terms of the mean fields as

$$\begin{aligned}\mathcal{L}_V = &- g_{\omega NN}\sum_{\alpha j}\bar{N}_{\alpha j}\gamma^0\omega N_{\alpha j} - g_{\rho NN}\sum_{\alpha j}\bar{N}_{\alpha j}\gamma^0\frac{\tau_3}{2}\rho N_{\alpha j} \\ &+ \frac{1}{2}m_\omega^2\omega^2 + \frac{1}{2}m_\rho^2\rho^2 + \lambda_{\omega\rho}g_{\omega NN}^2 g_{\rho NN}^2\omega^2\rho^2 \,.\end{aligned} \tag{76}$$

with

$$g_{\omega NN} = (a_{VNN} + a_{0NN})g_\omega \,, \tag{77}$$

$$g_{\rho NN} = a_{VNN}g_\rho \,. \tag{78}$$

It is crucial to note that $\lambda_{\omega\rho} \geq 0$ is required to realize $\omega = \rho = 0$ in vacuum. To show it, we start from the vector meson potential in vacuum given as

$$V_V \equiv -\frac{1}{2}m_\omega^2\omega^2 - \frac{1}{2}m_\rho^2\rho^2 - \lambda_{\omega\rho}g_{\omega NN}^2 g_{\rho NN}^2\omega^2\rho^2 \,. \tag{79}$$

The vacuum expectation values of the vector meson fields are chosen at the stationary point of V_V with minimal energy. The stationary conditions are given by

$$\begin{aligned}\frac{\partial V_V}{\partial\omega} &= \omega[m_\omega^2 + 2\lambda_{\omega\rho}g_{\omega NN}^2 g_{\rho NN}^2\rho^2] = 0 \,, \\ \frac{\partial V_V}{\partial\rho} &= \rho[m_\rho^2 + 2\lambda_{\omega\rho}g_{\omega NN}^2 g_{\rho NN}^2\omega^2] = 0 \,,\end{aligned} \tag{80}$$

leading to two distinct stationary points,

$$(\omega^2, \rho^2) = (0,0), (-\frac{m_\rho^2}{2\lambda_{\omega\rho}g_{\omega NN}^2 g_{\rho NN}^2}, -\frac{m_\omega^2}{2\lambda_{\omega\rho}g_{\omega NN}^2 g_{\rho NN}^2}) \,. \tag{81}$$

Then, the values of potential at stationary points are

$$V_V = \begin{cases} 0, & \text{for } (\omega^2,\rho^2) = (0,0) \,, \\ \frac{m_\omega^2 m_\rho^2}{4\lambda_{\omega\rho}g_{\omega NN}^2 g_{\rho NN}^2}, & \text{for } (\omega^2,\rho^2) = (-\frac{m_\rho^2}{2\lambda_{\omega\rho}g_{\omega NN}^2 g_{\rho NN}^2}, -\frac{m_\omega^2}{2\lambda_{\omega\rho}g_{\omega NN}^2 g_{\rho NN}^2}) \,. \end{cases} \tag{82}$$

In the present model, vanishing vacuum expectation values of the vector meson fields are required at zero density due to the Lorentz-invariance of the vacuum. Consequently, we must require $\lambda_{\omega\rho} \geq 0$ here, such that $(\omega^2, \rho^2) = (0,0)$ minimizes the effective potential V_V in vacuum.

Then, the thermodynamic potential for the nucleons is written as

$$\Omega_N = -2\sum_{\alpha=\pm, j=\pm}\int^{k_f}\frac{d^3p}{(2\pi)^3}\Big[\mu_j^* - \omega_{\alpha j}\Big], \tag{83}$$

where $\alpha = \pm$ denotes the parity and $j = \pm$ the iso-spin of nucleons ($j = +$ for proton and $j = -$ for neutron). μ_j^* is the effective chemical potential given by

$$\mu_j^* \equiv (\mu_B - g_{\omega NN}\omega) + \frac{j}{2}(\mu_I - g_{\rho NN}\rho)\,, \tag{84}$$

and $\omega_{\alpha j}$ is the energy of the nucleon defined as $\omega_{\alpha j} = \sqrt{(\vec{p})^2 + (m^*_{\alpha j})^2}$, where $\vec{p}$ and $m^*_{\alpha j}$ are the momentum and the effective mass of the nucleon. The effective mass $m^*_{\alpha j}$ is given by

$$m^*_{\alpha j} = \frac{1}{2}\left[\sqrt{(g_1+g_2)^2(\sigma - ja)^2 + 4m_0^2} + \alpha(g_1 - g_2)(\sigma - ja)\right]. \tag{85}$$

We note that the masses of proton and neutron become non-degenerate in the asymmetric matter due to the non-zero mean field of $a_0(980)$.

The entire thermodynamic potential for hadronic matter is expressed as

$$\begin{aligned}\Omega_H = \Omega_N & \\ & - \frac{\bar{\mu}_\sigma^2}{2}\sigma^2 - \frac{\bar{\mu}_a^2}{2}a^2 + \frac{\lambda_4}{4}(\sigma^4 + a^4) + \frac{\gamma_4}{2}\sigma^2 a^2 \\ & - \frac{\lambda_6}{6}(\sigma^6 + 15\sigma^2 a^4 + 15\sigma^4 a^2 + a^6) + \lambda_6^{'}(\sigma^2 a^4 + \sigma^4 a^2) \\ & - m_\pi^2 f_\pi \sigma - \frac{1}{2}m_\omega^2\omega^2 - \frac{1}{2}m_\rho^2\rho^2 - \lambda_{\omega\rho}g_{\omega NN}^2 g_{\rho NN}^2\omega^2\rho^2 \\ & - \Omega_0\,,\end{aligned} \tag{86}$$

where we subtracted the potential at the vacuum

$$\Omega_0 \equiv -\frac{\bar{\mu}_\sigma^2}{2}f_\pi^2 + \frac{\lambda_4}{4}f_\pi^4 - \frac{\lambda_6}{6}f_\pi^6 - m_\pi^2 f_\pi^2\,. \tag{87}$$

4.2. Determination of Model Parameters

In the present model, there are seven parameters in the meson potential, μ_σ^2, $\mu_a^2 = \mu_\sigma^2 - K$, λ_4, γ_4, λ_6, λ_6', and $\lambda_{\omega\rho}$, in addition to the meson masses m_π, m_ω, m_ρ, and the pion decay constant f_π. We also have four parameters, g_1, g_2, $g_{\omega NN}$, and $g_{\rho NN}$ for the couplings of mesons to baryons. As in Section 2, we use the physical values of three masses m_π, m_ω, and m_ρ, together with the pion decay constant f_π as listed in Table 2. In addition, we use the masses of $a_0(980)$ and η mesons listed in Table 10 as inputs. Similarly to Section 2, we determine the values of μ_σ^2, λ_4, λ_6 and $g_{\omega NN}$ from the saturation properties: the saturation density n_0, the binding energy B_0, and the incompressibility K_0 summarized in Table 1, combined with the vacuum condition given in Equation (52). g_1 and g_2 are determined from the vacuum mass of nucleon $N(939)$ and its parity partner $N^*(1535)$. The resultant values are same as those shown in Table 3. Then, the parameters K and γ_4 are determined from the meson masses and the other parameters as

$$\begin{aligned} K &= m_\eta^2 - m_\pi^2\,, \\ \gamma_4 &= \frac{m_{a_0}^2 + (5\lambda_6 - 2\lambda_6')f_\pi^4 + \bar{\mu}_a^2}{f_\pi^2}\,, \end{aligned} \tag{88}$$

where m_η and m_{a_0} are the masses of η and a_0.

Table 10. Values of masses of $a_0(980)$ and η mesons in unit of MeV.

m_{a_0}	m_η
980	550

As we stated in the previous subsection, we take $\lambda_6' = 0$ for a while. The resultant values of $\bar{\mu}_a^2$ and γ_4 corresponding to a given m_0 are presented in Table 11.

Table 11. Values of parameters $\bar{\mu}_a^2$ and γ_4 for several choices of m_0 and K_0 with $\lambda_6' = 0$.

	m_0 [MeV]	600	700	800	900
$K_0 = 215$ MeV	$\bar{\mu}_a^2/f_\pi^2$	−9.40	−11.79	−19.43	−30.27
	γ_4	185.59	177.94	144.51	90.62
$K_0 = 240$ MeV	$\bar{\mu}_a^2/f_\pi^2$	−10.95	−13.93	−21.08	−31.24
	γ_4	176.81	164.81	133.38	83.05

To demonstrate the effect of $a_0(980)$ on the matter, we consider both the a_0 model with vector-meson mixing ($\lambda_{\omega\rho} \neq 0$) and that without the mixing ($\lambda_{\omega\rho} = 0$). In the a_0 model without vector meson mixing, parameter $g_{\rho NN}$ is determined from the symmetry energy at the saturation density S_0, while the slope parameter L_0 is computed from the model as an output.

Table 12 shows the values of $g_{\rho NN}$ together with L_0. We note that the slope parameters are much larger than the recently accepted value $L_0 = 57.7 \pm 19$ MeV [72]. We also note that the effect of K_0 on the value of L_0 is larger when we include the a_0 meson into the model. The value of L_0 with different S_0 is shown in Table 13.

Table 12. The values of $g_{\rho NN}$ and slope parameter L_0 in the a_0 model without vector meson mixing, for several choices of m_0 and K_0 with $\lambda_6' = 0$. $S_0 = 31$ MeV.

	m_0 [MeV]	600	700	800	900
$K_0 = 215$ MeV	$g_{\rho NN}$	12.52	11.20	9.94	8.90
	L_0 [MeV]	120.14	105.21	97.05	87.65
$K_0 = 240$ MeV	$g_{\rho NN}$	12.47	11.16	9.90	8.86
	L_0 [MeV]	126.58	108.78	98.67	87.75
$K_0 = 260$ MeV	$g_{\rho NN}$	12.43	11.13	9.86	8.83
	L_0 [MeV]	131.19	111.45	99.86	87.75

Table 13. Values of $g_{\rho NN}$ and slope parameter L_0 in the a_0 model without vector meson mixing, for several choices of m_0 and S_0 with $\lambda_6' = 0$. $K_0 = 215$ MeV.

	m_0 [MeV]	600	700	800	900
$S_0 = 24$ MeV	$g_{\rho NN}$	11.37	9.9	8.45	7.2
	L_0 [MeV]	99.14	84.21	76.05	66.65
$S_0 = 31$ MeV	$g_{\rho NN}$	12.52	11.2	9.94	8.9
	L_0 [MeV]	120.14	105.21	97.05	87.65
$S_0 = 36$ MeV	$g_{\rho NN}$	13.28	12.04	10.88	9.94
	L_0 [MeV]	135.14	120.21	112.05	102.65

For making the slope parameter consistent with $L_0 = 57.7 \pm 19$ MeV, we include the vector meson mixing interaction, which allows us to reduce L_0. In the a_0 model with vector meson mixing, the parameters $g_{\rho NN}$ and $\lambda_{\omega\rho}$ are determined by fitting them to the symmetry energy S_0, as well as the slope parameter L_0. To reproduce the matter for recent accepted value of $L_0 = 57.7 \pm 19$ MeV, we compute our results for $L_0 = 40$–80 MeV. The resultant parameters are shown in Tables 14 and 15. Here, we only show the results for $\lambda_6' = 0$ because the values of the parameters for $\lambda_6' = \pm\lambda_6$ are similar to the values listed in Tables 14 and 15.

Table 14. Values of $g_{\rho NN}$ for several choices of m_0, L_0, with $\lambda_6' = 0$. Vector meson mixing is considered.

	m_0 [MeV]	600	700	800	900
$K_0 = 215$ MeV	$L_0 = 40$ MeV	15.34	13.78	12.59	11.42
	$L_0 = 50$ MeV	14.88	13.27	11.97	10.72
	$L_0 = 60$ MeV	14.46	12.81	11.44	10.13
	$L_0 = 70$ MeV	14.08	12.39	10.97	9.63
	$L_0 = 80$ MeV	13.72	12.02	10.55	9.19
$K_0 = 240$ MeV	$L_0 = 40$ MeV	15.63	13.96	12.68	11.41
	$L_0 = 50$ MeV	15.14	13.42	12.04	10.7
	$L_0 = 60$ MeV	14.69	12.94	11.49	10.11
	$L_0 = 70$ MeV	14.28	12.51	11.0	9.6
	$L_0 = 80$ MeV	13.9	12.11	10.58	9.16

Table 15. Values of $\lambda_{\omega\rho}$ for several choices of m_0, L_0, with $\lambda_6' = 0$. Vector meson mixing is considered.

	m_0 [MeV]	600	700	800	900
$K_0 = 215$ MeV	$L_0 = 40$ MeV	0.0254	0.0818	0.3191	2.8164
	$L_0 = 50$ MeV	0.0222	0.0693	0.2632	2.2253
	$L_0 = 60$ MeV	0.0191	0.0567	0.2072	1.6342
	$L_0 = 70$ MeV	0.0159	0.0442	0.1513	1.0431
	$L_0 = 80$ MeV	0.0127	0.0316	0.0954	0.4519
$K_0 = 240$ MeV	$L_0 = 40$ MeV	0.0252	0.0761	0.2914	2.4593
	$L_0 = 50$ MeV	0.0223	0.065	0.2418	1.9443
	$L_0 = 60$ MeV	0.0194	0.054	0.1921	1.4293
	$L_0 = 70$ MeV	0.0165	0.0429	0.1424	0.9142
	$L_0 = 80$ MeV	0.0135	0.0318	0.0927	0.3992

4.3. Effect of $a_0(980)$ to Symmetry Energy in Model Without Vector Meson Mixing

The $a_0(980)$ meson should affect the properties of the matter via the asymmetry of the matter. Therefore, we expect that symmetry energy is essential to study the effect of $a_0(980)$ meson to the matter. In the following, we study how the inclusion of the $a_0(980)$ meson affects the symmetry energy.

In the present model, the symmetry energy S(n_B) for a given density n_B is expressed as

$$\begin{aligned} S(n_B) &= \frac{n_B}{8}\frac{\partial \mu_I}{\partial n_I}\Big|_{n_I=0} \\ &= \frac{(k_+^*)^2}{6\mu_+^*} + \frac{n_B}{2}\frac{(g_{\rho NN}/2)^2}{m_\rho^2} - \frac{n_B}{4}\frac{m_+^*}{\mu_+^*}\frac{\partial m_{+n}^*}{\partial n_I}\Big|_{n_I=0}, \end{aligned} \tag{89}$$

where $\mu_+^* \equiv \mu_p^*|_{n_I=0} = \mu_n^*|_{n_I=0}$ is the effective chemical potential for $N(939)$ in the symmetric matter, $k_+^* \equiv \sqrt{(\mu_p^*)^2 - (m_{+p}^*)^2}|_{n_I=0} = \sqrt{(\mu_n^*)^2 - (m_{+n}^*)^2}|_{n_I=0}$ the corresponding Fermi momentum, $m_+^* \equiv m_{+p}^*|_{n_I=0} = m_{+n}^*|_{n_I=0}$ the mass. In Equation (89), there are three contributions to the symmetry energy: the nucleon contribution, the ρ meson contribution, and the a_0 meson contribution.

The nucleon contribution $S_N(n_B)$ is given by

$$S_N(n_B) \equiv \frac{(k_+^*)^2}{6\mu_+^*}, \tag{90}$$

which arises from the effective kinetic contribution of nucleons. Figure 4 shows $S_N(n_B)$ for $m_0 = 600$–900 MeV with $K_0 = 215, 240$ MeV. It is observed that $S_N(n_B)$ increases with density, as the effective kinetic energy of nucleons rises with density. Additionally, it is noted that $S_N(n_B)$ is larger for smaller m_0 due to the stiffening of matter for smaller m_0. It can be also seen that $S_N(n_B)$ is larger for larger K_0. However, the change in K_0 has little effect on $S_N(n_B)$. We note that, since $S_N(n_B)$ arises from the effective kinetic contribution of a nucleon, $S_N(n_B)$ is not affected by the inclusion of a_0 meson.

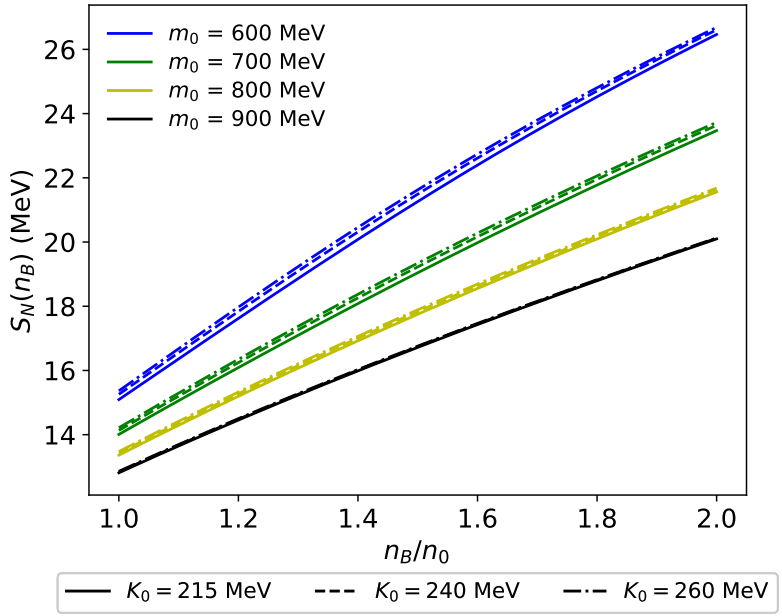

Figure 4. Nucleon contribution $S_N(n_B)$ for $m_0 = 600$–900 MeV. Solid, dashed, and dash-dot curves represent $S_N(n_B)$ with $K_0 = 215, 240, 260$ MeV, respectively.

The contribution from the $a_0(980)$ meson is expressed as

$$S_{a_0}(n_B) \equiv -\frac{n_B}{4}\frac{m_+^*}{\mu_+^*}\frac{\partial m_{+n}^*}{\partial n_I}\Big|_{n_I=0}. \tag{91}$$

Figure 5 shows S_{a_0} computed in the present model. We note that S_{a_0} is negative and, thus, reduces the total symmetry energy $S(n_B)$. This is because $\frac{\partial m_{+n}^*}{\partial n_I}|_{n_I=0}$ is always positive, as shown in Figure 6. Intuitively, this can be understood from the dependence of m_{+n}^* on the mean field a given in Equation (85). If we vary the mean field a, m_{+n}^* will also change correspondingly. However, the effective chemical potential μ_n^* does not depend on the mean field a directly, as we can see from Equation (84). This change in the effective mass m_{+n}^* due to the mean field a leads to a change in the momentum of the neutron $k_{+n} = \sqrt{(\mu_n^*)^2 - (m_{+n}^*)^2}$. When $n_I = (n_p - n_n)/2$ is increased for a fixed n_B, the density of the neutron n_n and, thus, the momentum k_{+n} is decreased. Accordingly, the effective mass of the neutron is increasing as n_I increase, causing a positive $\frac{\partial m_{+n}}{\partial n_I}|_{n_I=0}$. Therefore, the $a_0(980)$ meson contribution $S_{a_0}(n_B)$ reduces the total symmetry energy $S(n_B)$ in the present model. We also find that the $a_0(980)$ effect on the symmetry energy is stronger for smaller m_0. This is because the coupling constants of $a_0(980)$ meson to the nucleon, g_1 and g_2, are larger for smaller m_0, as shown in Table 3. As a result, the symmetry energy becomes larger by $a_0(980)$ meson more when m_0 is smaller. In addition, we note that the $a_0(980)$ effect on the symmetry energy is decreasing as the density increases since $\frac{\partial m_{+n}}{\partial n_I}|_{n_I=0}$ decreases. We also observe that K_0 has a larger effect on S_{a_0} due to the effect of K_0 on the coupling constants of a_0 meson, as indicated in Tables 3 and 11. Since the effect of the a_0 meson becomes smaller as the density increases, S_{a_0} becomes less negative and spreads at higher densities. We also note that the difference of S_{a_0} with different K_0 becomes smaller as m_0 increase due to a weaker a_0 meson effect. Notice that this contribution does not exist in models without the a_0 meson.

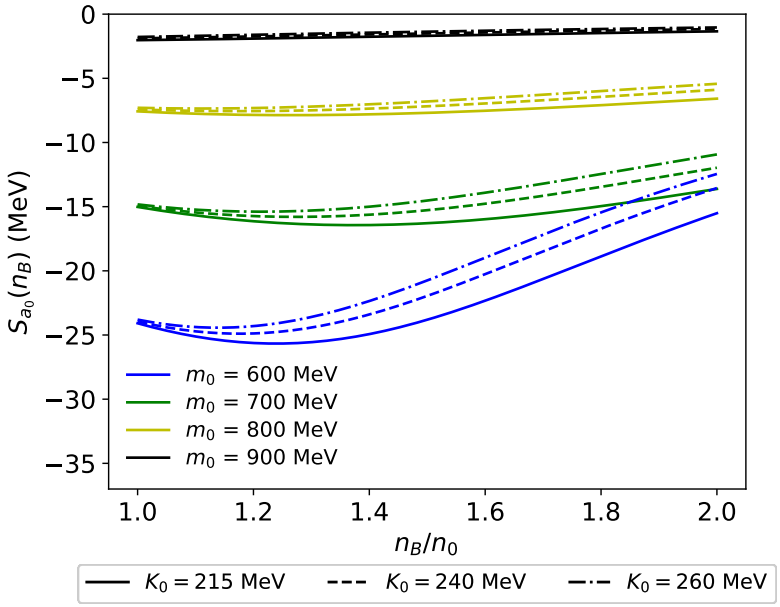

Figure 5. a_0 meson contribution to the symmetry energy $S_{a_0}(n_B)$ for m_0 = 600–900 MeV. Solid, dashed, and dash-dot curves represent $S_{a_0}(n_B)$ with $K_0 = 215, 240, 260$ MeV, respectively.

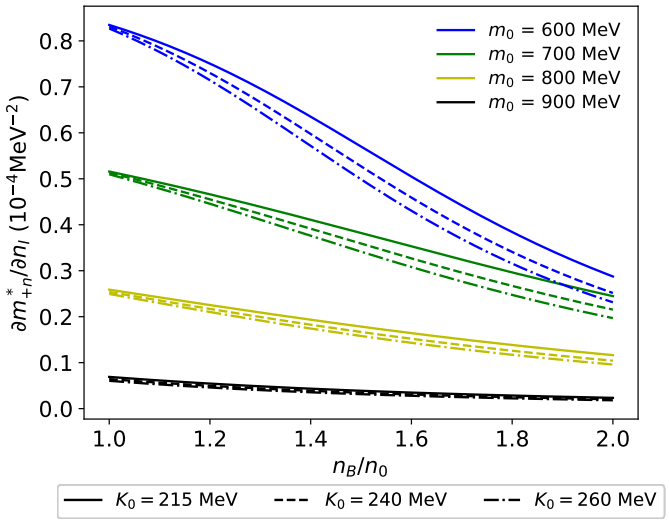

Figure 6. $\frac{\partial m^*_{+n}}{\partial n_I}|_{n_I=0}$ for m_0 = 600–900 MeV. Solid, dashed, and dash-dot curves represent $\frac{\partial m^*_{+n}}{\partial n_I}|_{n_I=0}$ with $K_0 = 215, 240, 260$ MeV, respectively.

The ρ meson contribution is given by

$$S_\rho(n_B) \equiv \frac{n_B}{2}\frac{(g_{\rho NN}/2)^2}{m_\rho^2}\,. \tag{92}$$

This shows that the contribution is always positive and, thus, provides repulsive force to the matter. Figure 7 shows the behavior of $S_\rho(n_B)$ for m_0 = 600–900 MeV with $K_0 = 215$, 240 MeV. It is noteworthy that $S_\rho(n_B)$ is directly proportional to the baryon density n_B, rendering it an increasing function with density. We also note that $S_\rho(n_B)$ exhibits larger values for heavier m_0. This is understood as follows: at the saturation density, the symmetry energy S_0 is fixed to be 31 MeV. Since the total symmetry energy is given by Equation (89), a larger m_0 corresponds to a smaller $S_N(n_0)$ and, consequently, a larger $S_\rho(n_0)$. This larger $S_\rho(n_0)$ yields a larger coupling constant $g_{\rho NN}$ for larger m_0. As a result, $S_\rho(n_B)$ is larger for larger m_0 at density higher than the saturation density. Figure 7 also shows that K_0 has

little effect on S_ρ. We note that S_N and S_{a_0} is determined from K_0. Then, we obtain $S_\rho(n_B)$ from S_0, S_N and S_{a_0}. Since S_N and S_{a_0} are larger as K_0 increases, these two contributions compensate with S_ρ to maintain $S_0 = 31$ MeV at $n_B = n_0$. Thus, S_ρ is smaller as K_0 increases, which is opposite to S_N and S_{a_0}. We also observe that the value of S_ρ for the present model is very large compared with the value of model without a_0 meson. This is because the ρ meson coupling is much larger in the present model due to the attractive interaction of $a_0(980)$ when comparing to the model without a_0 meson.

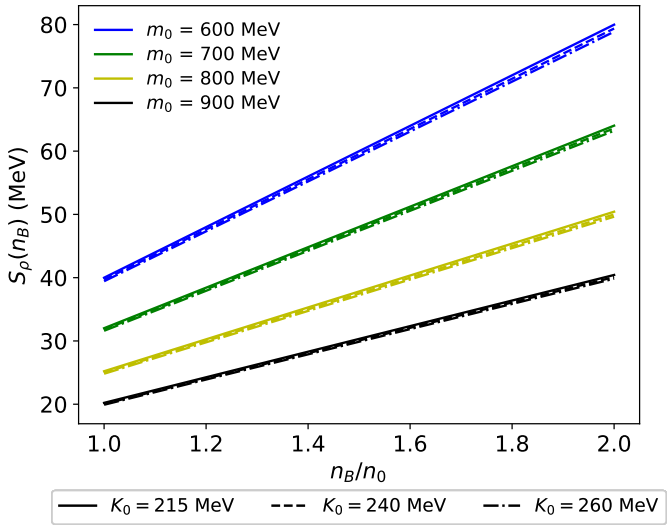

Figure 7. ρ meson contribution $S_\rho(n_B)$ in a_0 model for $m_0 = 600$–900 MeV and $\lambda_6' = 0$. Solid, dashed, and dash-dot curves represent $S_\rho(n_B)$ with $K_0 = 215, 240, 260$ MeV, respectively.

Based on the above properties of three contributions, the symmetry energy can be understood as a result of the competition between the repulsive ρ meson interaction and the attractive $a_0(980)$ interaction, in addition to the kinetic contribution from the nucleons. On the other hand, in the model without a_0 meson, only repulsive contributions exist. Since the symmetry energy at the saturation density is fixed as $S_0 = 31$ MeV in the both models with and without $a_0(980)$ meson, the ρ meson coupling $g_{\rho NN}$ is strengthened by the existence of the attractive $a_0(980)$ contribution in the model with a_0 comparing to the model without a_0. Actually, it is clear from Tables 3 and 12 that $g_{\rho NN}$ is larger in the a_0 model than in the no-a_0 model for a fixed m_0. Figure 8 shows the symmetry energy for $m_0 = 600$–900 MeV and $K_0 = 215$ MeV, with the results of the model with a_0 meson and without a_0 meson are shown in solid curve and dashed curve, respectively. We observe that the symmetry energy is indeed stiffened by the existence of $a_0(980)$. Furthermore, the difference of the symmetry energy between the models is larger for smaller m_0 because the coupling to the a_0 meson is stronger, as indicated by Table 3. At $n_B = 2n_0$, the symmetry energy $S(2n_0)$ is enlarged by $a_0(980)$ meson as large as $\sim$60% or more in the present model depending on the choice of input parameters.

In Figure 9, we compare the total symmetry energy with different choices of K_0, and the results show that the symmetry energy is not sensitive to the value of K_0 because the effect of K_0 to the total symmetry energy is canceled by the compensation between S_N, S_{a_0}, and S_ρ.

The effect of S_0 to the total symmetry energy $S(n_B)$ is also studied. Figure 10 shows the difference of the symmetry energy $S(n_B) - S_0$. We note that S_0 has large impact to the symmetry energy, since S_0 affects the determination of $g_{\rho NN}$. As expected, larger S_0 results in larger $S(n_B)$.

In addition, we investigate the effect of higher-order terms in the large N_c expansion for the six-point interaction on the symmetry energy by taking $\lambda_6' = \pm\lambda_6$. The results of the symmetry energies with different values of λ_6' are shown in Figure 11. We can see

that the difference between the symmetry energies for models with the same m_0 is small, which indicates that the effect of λ_6' on the symmetry energy is small. Notice also that the difference becomes smaller for larger m_0, due to a smaller $a_0(980)$ effect.

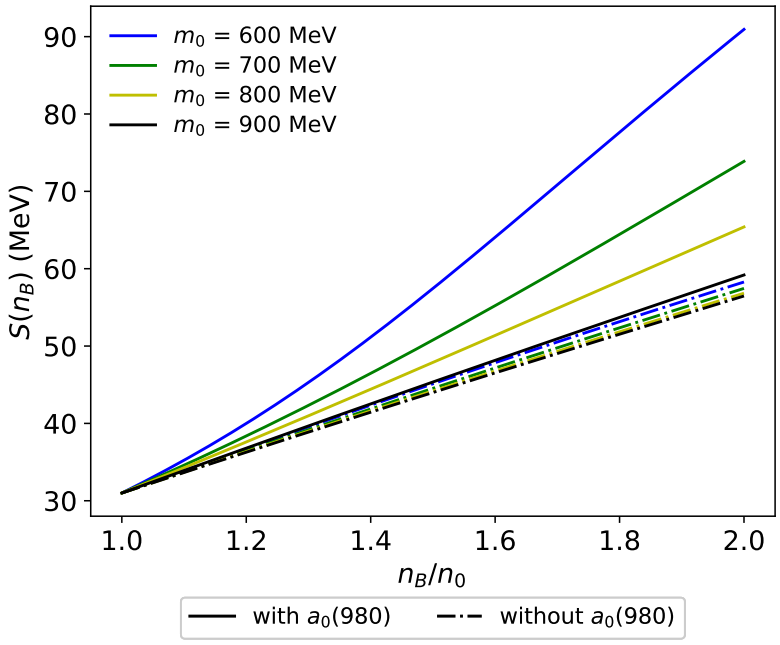

Figure 8. Symmetry energy $S(n_B)$ for $m_0 = 600$–900 MeV, $K_0 = 215$ MeV, and $\lambda_6' = 0$. Solid curves represent the $S(n_B)$ of the model, including $a_0(980)$ with $\lambda_6' = 0$, while the dash-dot curves show the results of the model without $a_0(980)$.

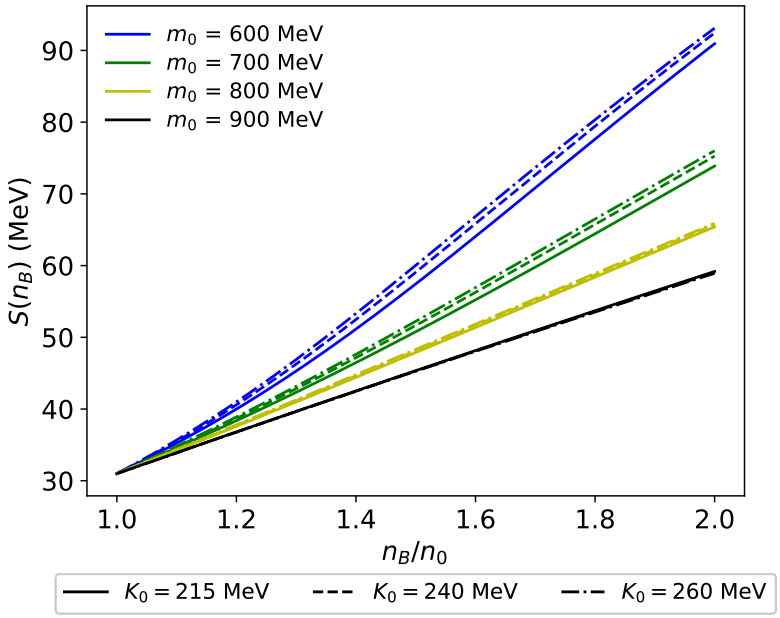

Figure 9. Symmetry energy $S(n_B)$ for $m_0 = 600$–900 MeV, $\lambda_6' = 0$, with different choices of K_0 compared. Solid, dashed, and dash-dot curves represent $S(n_B)$ with $K_0 = 215, 240, 260$ MeV, respectively.

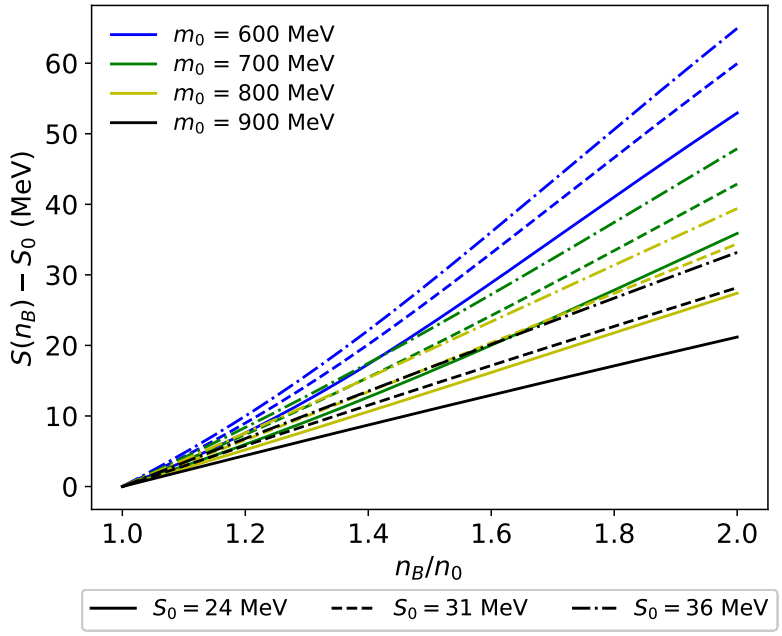

Figure 10. Difference of the symmetry energy $S(n_B) - S_0$ in a_0 model for $m_0 = 600$–900 MeV and $\lambda_6' = 0$. $K_0 = 215$ MeV. Solid, dashed, and dash-dot curves represent $S_\rho(n_B)$ with $S_0 = 24, 31,$ 36 MeV, respectively.

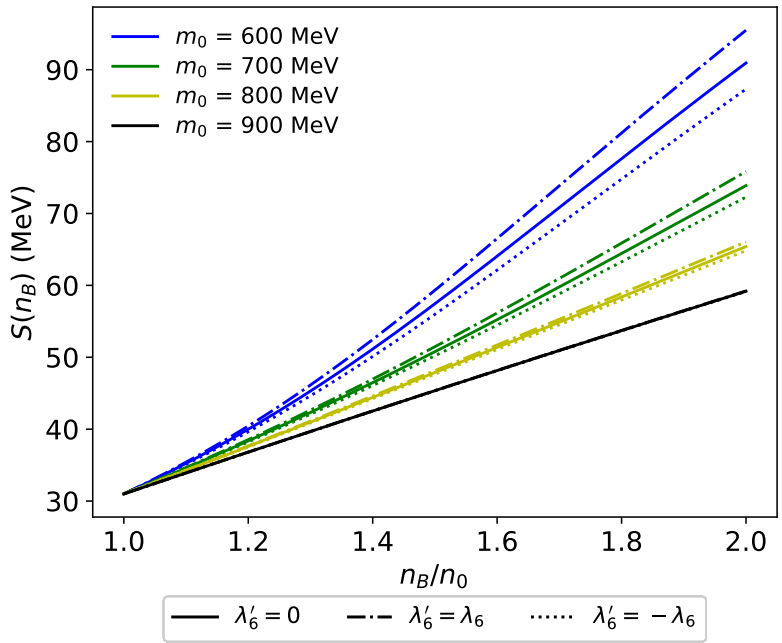

Figure 11. Symmetry energy $S(n_B)$ for $m_0 = 600$–900 MeV and $K_0 = 215$ MeV, with the effect of λ_6' compared. Solid, dash-dot, and dotted curves show the $S(n_B)$ with $\lambda_6' = 0, \lambda_6$, and $-\lambda_6$, respectively.

4.4. Symmetry Energy of a_0 Model with Vector Meson Mixing

As we see from the previous sections, PDM predicts a rather large slope parameter L_0, which does not seem compatible with the recently accepted value of $L_0 = 57.7 \pm 19$ MeV. In particular, the model with a_0 meson predicts a very large L_0, as well as the symmetry energy at density $n_B > n_0$. In order to soften the matter to reproduce the accepted value of L_0, we include the ω-ρ vector mixing term to reduce the stiffness of the matter in our model. In this section, we study the symmetry energy with vector meson mixing interaction.

In the current model, the symmetry energy $S(n_B)$ for a given density n_B is expressed as follows:

$$\begin{aligned} S(n_B) &= \frac{n_B}{8}\frac{\partial \mu_I}{\partial n_I}\Big|_{n_I=0} \\ &= \frac{(k_+^*)^2}{6\mu_+^*} + \frac{n_B}{2}\frac{(g_{\rho NN}/2)^2}{m_\rho^2 + (2\lambda_{\omega\rho} g_{\omega NN}^4 g_{\rho NN}^2 n_B^2/m_\omega^4)} - \frac{n_B}{4}\frac{m_+^*}{\mu_+^*}\frac{\partial m_{+n}^*}{\partial n_I}\Big|_{n_I=0}. \end{aligned} \tag{93}$$

Similarly to Equation (89), the symmetry energy is divided into sum of three contributions: the nucleon contribution $S_N(n_B)$, ρ meson contribution $S_\rho(n_B)$, and a_0 meson contribution $S_{a_0}(n_B)$. Notably, the nucleon contribution and a_0 meson contribution are unaffected by the vector meson mixing, since their related parameters are determined from symmetric matter properties. Therefore, the results of $S_N(n_B)$ and $S_{a_0}(n_B)$ are the same as given in Figures 4 and 5.

On the other hand, the ρ meson contribution receives a correction from the vector meson mixing interaction as

$$S_\rho(n_B) \equiv \frac{n_B}{2}\Big[\frac{(g_{\rho NN}/2)^2}{m_\rho^2 + (2\lambda_{\omega\rho} g_{\omega NN}^4 g_{\rho NN}^2 n_B^2/m_\omega^4)}\Big], \tag{94}$$

where the ρ meson appears to have an effective mass $(m_\rho^*)^2 = m_\rho^2 + (2\lambda_{\omega\rho} g_{\omega NN}^4 g_{\rho NN}^2 n_B^2/m_\omega^4)$ exhibiting density-dependence. We note that the ω meson influences the symmetry energy through $2\lambda_{\omega\rho} g_{\omega NN}^4 g_{\rho NN}^2 n_B^2/m_\omega^4$ in the denominator. Given that $\lambda_{\omega\rho} > 0$, as shown in Section 4.1, the ω-ρ mixing term always reduces the symmetry energy. The density dependence of S_ρ is illustrated in Figure 12. It is observed that S_ρ increases with rising n_B in the low-density region, but decreases in the high-density region. This is understood as follows: in the low-density region where $m_\rho^2 \gg 2\lambda_{\omega\rho} g_{\omega NN}^4 g_{\rho NN}^2 n_B^2/m_\omega^4$, the density dependence of $S_\rho(n_B)$ is primarily determined by the pre-factor n_B. In the high density region, on the other hand, the denominator is dominated by $2\lambda_{\omega\rho} g_{\omega NN}^4 g_{\rho NN}^2 n_B^2/m_\omega^4$, which leads to $S_\rho(n_B) \propto 1/n_B$. As a result, the behavior of S_ρ smoothly transforms from $\sim n_B \to \sim 1/n_B$. We also observe that the value of K_0 has larger influence to $S_\rho(n_B)$ due to the vector meson mixing. $S_\rho(n_B)$ receives a extra correction from $g_{\omega NN}$ coming from the vector meson mixing as we read from Equation (94). Since the repulsive $g_{\omega NN}$ coupling increase as K_0 becomes larger, $S_\rho \sim 1/g_{\omega NN}^4$ is smaller with larger K_0 and further spread at higher densities.

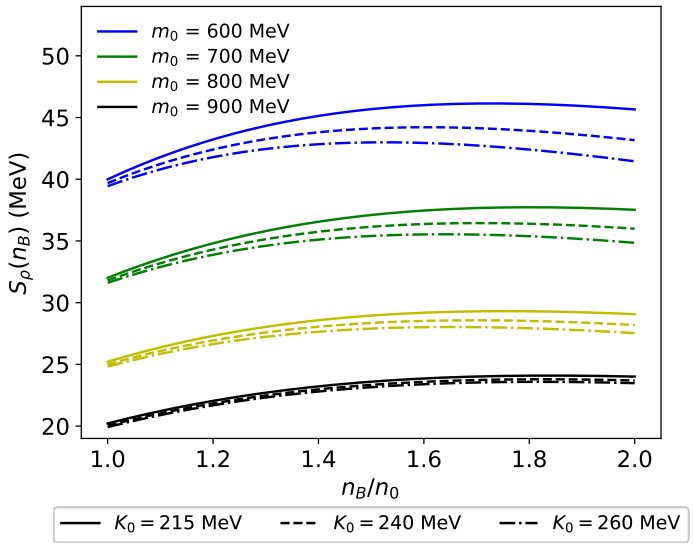

Figure 12. ρ meson contribution $S_\rho(n_B)$ in a_0 model for $m_0 = 600$–900 MeV, $\lambda_6' = 0$, and $L_0 = 60$ MeV. Solid, dashed, and dash-dot curves represent $S_\rho(n_B)$ with $K_0 = 215, 240, 260$ MeV, respectively.

Figure 13 shows the total symmetry energy $S(n_B)$ for $m_0 = 600$–900 MeV and $L_0 = 60$ MeV. For comparison, we also show the results of the no-a_0 model with vector meson mixing by dashed curves, as retrieved from Ref. [66]. We note that when the vector meson mixing is included, the slope of the symmetry energy is reduced in the high density region. We also observe that, in most cases, the symmetry energy is stiffened by the existence of $a_0(980)$, and the difference of the symmetry energy between two models is larger for smaller m_0. In the case of large m_0, such as $m_0 = 900$ MeV where the $a_0(980)$ meson effect is small, the softening effect of $\lambda_{\omega\rho}$ term overrides the stiffening effect from the $a_0(980)$ meson. As a result, the symmetry energy $S(n_B)$ is reduced even after the inclusion of a_0 meson. A similar reduction in the symmetry energy in the intermediate density region was also reported in Ref. [56], which includes both the scalar meson mixing and the vector meson mixing interactions in an RMF model with the presence of isovector-scalar meson.

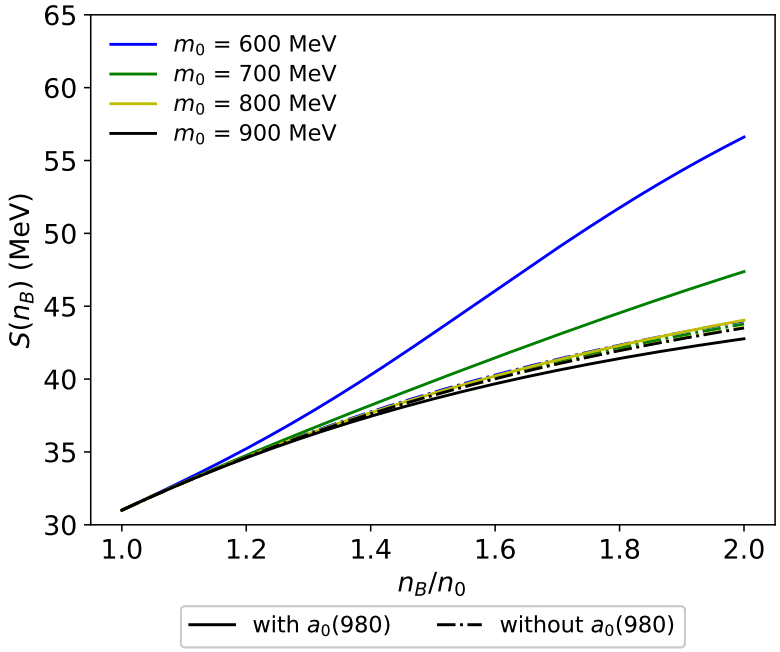

Figure 13. Symmetry energy $S(n_B)$ in a_0 model with vector meson mixing for $m_0 = 600$–900 MeV, $\lambda_6' = 0$, $K_0 = 215$ MeV, and $L_0 = 60$ MeV. Solid curves represent the $S(n_B)$ of the model, including $a_0(980)$ with $\lambda_6' = 0$, while the dash-dot curves show the results of the model without $a_0(980)$.

In Figure 14, we study the K_0 dependence of the symmetry energy. Similarly to the models introduced in the previous sections, K_0 has very little effect to the symmetry energy. Due to the extra correction of the vector meson mixing to S_ρ, the effect of K_0 is further suppressed due to the compensation of the effect of K_0 to S_N, S_{a_0}, and S_ρ.

In particular, the results of $m_0 = 700$ MeV and $L_0 = 60$ MeV from the present model is compared to the results of other mean field models such as FSU-δ6.7 [56] and B. Liu et al. [63], and density dependent RMF models such as DD-MEδ [65] in Figure 15. We observe that the vector meson mixing reduces the symmetry energy at high density similarly to the model with density dependent couplings without vector meson mixing interaction. In addition, our a_0 model without vector meson mixing predicts a large symmetry energy similarly to the RMF model without vector meson mixing, while the symmetry energy in models with vector meson mixing is effectively reduced.

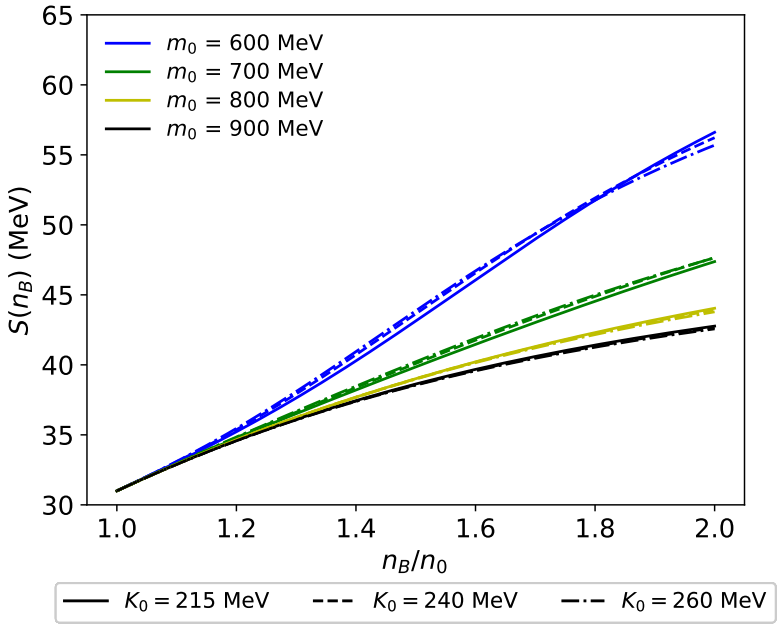

Figure 14. K_0 dependence of the symmetry energy $S(n_B)$ in the a_0 model with vector meson mixing for $\lambda_6' = 0$, and $L_0 = 60$ MeV. Solid, dashed, and dash-dot curves represent $S(n_B)$ with $K_0 = 215, 240,$ 260 MeV, respectively.

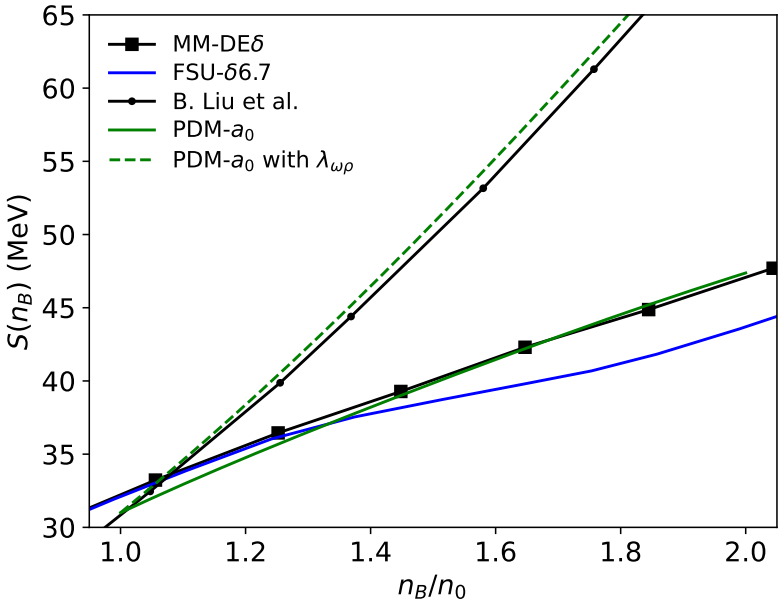

Figure 15. Comparison of the symmetry energy $S(n_B)$ of the present model with the ones of other models. The results from density dependent RMF model DD-MEδ [65] and RMF model from B. Liu et al. [63] and FSU-δ6.7 [56] are compared. The results from present model shown in the figure takes the typical value of $m_0 = 700$ MeV, $\lambda_6' = 0$, $K_0 = 215$ MeV, and $L_0 = 60$ MeV for result with vector meson mixing.

Finally, we compare the symmetry energy in the models with different λ_6' in Figure 16. As expected, the effect to symmetry energy is smaller than the effect of m_0, because λ_6' interactions are of sub-leading order in large N_c expansion.

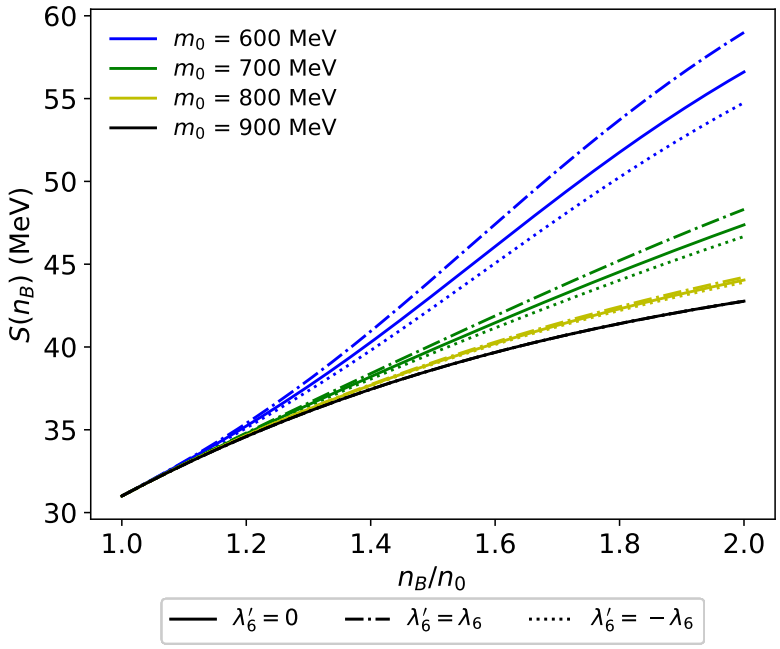

Figure 16. Symmetry energy $S(n_B)$ for $m_0 = 600$–900 MeV, $K_0 = 215$ MeV, and $L_0 = 60$ MeV with the effect of λ_6' compared. Solid, dash-dot, and dotted curves show the $S(n_B)$ with $\lambda_6' = 0, \pm\lambda_6$.

5. Summary

In this review, we summarized the recent studies on infinite nuclear matter and finite nuclei based on parity doublet models (PDMs). We first introduced a PDM, which is constructed in Ref. [19]. Under the mean field approximation, the nuclear properties such as slope parameter and symmetry energy were computed. In particular, we observed that the slope parameter is relatively larger than the recently accepted value $L_0 = 57.7 \pm 19$ MeV [72]. We also investigated the impact of the value of K_0 to the model. We found that the value of K_0 has little impact to the matter properties, such as the symmetry energy and slope parameter L_0 in the model without a_0 meson. We also studied the effect of S_0 to the slope parameter L_0. We find that the value of S_0 will affect the value of L_0 significantly.

We then considered the properties of some stable nuclei in the mean field approximation to pin down the value of the chiral invariant mass preferred by the nuclear binding energies and charge radii. We found that our results are closest to the experiments when we take $m_0 = 700$ MeV. We also calculated the neutron and proton masses in a nucleus and observed, as expected, that the neutron–proton mass difference becomes larger in an isospin asymmetric nucleus.

Then, we studied the effect of isovector scalar meson $a_0(980)$ to the matter. The isovector scalar meson provides the attractive force in the isovector channel, and is important in the asymmetric matter. We found that the inclusion of $a_0(980)$ has a very strong influence on the symmetry energy and slope parameter. We observed that the symmetry energy at densities $n_B > n_0$ is largely enhanced by the existence of $a_0(980)$. By analyzing the different contributions to the symmetry energy, we concluded that this enhancement is originated from the strengthening of the ρ meson coupling $g_{\rho NN}$. The $a_0(980)$ meson generates the attractive force in the isovector channel, which requires the repulsive force from ρ meson to be larger for reproducing the saturation property. As a result, a larger repulsive ρ interaction increases the symmetry energy at densities $n_B > n_0$. However, we also observed that this stiffening of nuclear matter produces a large slope parameter that is much larger than the recently accepted value suggested by other studies. Therefore, we introduced the ω-ρ mixing interaction to reduce the slope parameter in the model. It was found that the symmetry energy at density $n_B > n_0$ is reduced after the inclusion of ω-ρ

mixing interaction. Furthermore, we observed that the ω-ρ mixing interaction modifies the density dependence of the symmetry energy at density $n_B > n_0$. We also observed that the value of K_0 has relatively large impact on the a_0 contribution to symmetry energy S_{a_0} and L_0 due to the effect of K_0 to the a_0 meson. However, similarly to the case of model without the a_0 meson, K_0 has limited effect to the total symmetry energy $S(n_B)$ because of the compensation of the K_0 effect between S_N, S_{a_0}, and S_ρ. The effect is further suppressed when vector meson mixing effect is included. We also investigated the effect of S_0 to the total symmetry energy. As expected, the value of S_0 has large impact to the ρ meson coupling $g_{\rho NN}$ and thus the symmetry energy. There are also some microscopic nuclear force models in, e.g., Refs. [77–79]. It would be also interesting to compare the result of the present model to the results of these models.

We expect that future experiments on the study of symmetry energy at higher densities will provide further constraints on the chiral invariant mass of the nucleon. We also expect that $a_0(980)$ will have a significant influence on asymmetric nuclei. It would be interesting to study finite nuclei using the extended PDM including the $a_0(980)$ meson, which may give new information to constraints on the chiral invariant mass of the nucleon and the behavior of nucleon mass in dense matter. We leave this as future project.

Author Contributions: Writing—original draft preparation, Y.-K.K., Y.K., and M.H.; writing—review and editing, Y.-K.K., Y.K., and M.H. All authors have read and agreed to the published version of the manuscript.

Funding: This work was supported in part by the Institute for Basic Science (IBS-R031-D1) (YK), JSPS KAKENHI Grant Nos. 20K03927, 23H05439 and 24K07045 (MH).

Data Availability Statement: Data is contained within the article.

Acknowledgments: We thank Jie Meng for providing us the RCHB code.

Conflicts of Interest: The authors declare no conflicts of interest.

References

1. Aarts, G.; Allton, C.; Hands, S.; Jäger, B.; Praki, C.; Skullerud, J.I. Nucleons and parity doubling across the deconfinement transition. *Phys. Rev. D* **2015**, *92*, 014503. [CrossRef]
2. Aarts, G.; Allton, C.; De Boni, D.; Hands, S.; Jäger, B.; Praki, C.; Skullerud, J.I. Light baryons below and above the deconfinement transition: Medium effects and parity doubling. *J. High Energy Phys.* **2017**, *2017*, 34. [CrossRef]
3. DeTar, C.; Kunihiro, T. Linear sigma model with parity doubling. *Phys. Rev. D* **1989**, *39*, 2805–2808. [CrossRef]
4. Kim, J.; Lee, S.H. Masses of hadrons in the chiral symmetry restored vacuum. *Phys. Rev. D* **2022**, *105*, 014014. [CrossRef]
5. Jido, D.; Oka, M.; Hosaka, A. Chiral Symmetry of Baryons. *Prog. Theor. Phys.* **2001**, *106*, 873–908. [CrossRef]
6. Yamazaki, T.; Harada, M. Chiral partner structure of light nucleons in an extended parity doublet model. *Phys. Rev. D* **2019**, *99*, 034012. [CrossRef]
7. Hatsuda, T.; Prakash, M. Parity Doubling of the Nucleon and First Order Chiral Transition in Dense Matter. *Phys. Lett. B* **1989**, *224*, 11–15. [CrossRef]
8. Zschiesche, D.; Tolos, L.; Schaffner-Bielich, J.; Pisarski, R.D. Cold, dense nuclear matter in a SU(2) parity doublet model. *Phys. Rev. C* **2007**, *75*, 055202. [CrossRef]
9. Dexheimer, V.; Schramm, S.; Zschiesche, D. Nuclear matter and neutron stars in a parity doublet model. *Phys. Rev. C* **2008**, *77*, 025803. [CrossRef]
10. Dexheimer, V.; Pagliara, G.; Tolos, L.; Schaffner-Bielich, J.; Schramm, S. Neutron stars within the SU(2) parity doublet model. *Eur. Phys. J. A* **2008**, *38*, 105–113. [CrossRef]
11. Sasaki, C.; Mishustin, I. Thermodynamics of dense hadronic matter in a parity doublet model. *Phys. Rev. C* **2010**, *82*, 035204. [CrossRef]
12. Sasaki, C.; Lee, H.K.; Paeng, W.G.; Rho, M. Conformal anomaly and the vector coupling in dense matter. *Phys. Rev. D* **2011**, *84*, 034011. [CrossRef]
13. Gallas, S.; Giacosa, F.; Pagliara, G. Nuclear matter within a dilatation-invariant parity doublet model: The role of the tetraquark at nonzero density. *Nucl. Phys. A* **2011**, *872*, 13–24. [CrossRef]
14. Paeng, W.G.; Lee, H.K.; Rho, M.; Sasaki, C. Dilaton-Limit Fixed Point in Hidden Local Symmetric Parity Doublet Model. *Phys. Rev. D* **2012**, *85*, 054022. [CrossRef]
15. Steinheimer, J.; Schramm, S.; Stocker, H. The hadronic SU(3) Parity Doublet Model for Dense Matter, its extension to quarks and the strange equation of state. *Phys. Rev. C* **2011**, *84*, 045208. [CrossRef]

16. Dexheimer, V.; Steinheimer, J.; Negreiros, R.; Schramm, S. Hybrid Stars in an SU(3) parity doublet model. *Phys. Rev. C* **2013**, *87*, 015804. [CrossRef]
17. Paeng, W.G.; Lee, H.K.; Rho, M.; Sasaki, C. Interplay between ω-nucleon interaction and nucleon mass in dense baryonic matter. *Phys. Rev. D* **2013**, *88*, 105019. [CrossRef]
18. Benic, S.; Mishustin, I.; Sasaki, C. Effective model for the QCD phase transitions at finite baryon density. *Phys. Rev. D* **2015**, *91*, 125034. [CrossRef]
19. Motohiro, Y.; Kim, Y.; Harada, M. Asymmetric nuclear matter in a parity doublet model with hidden local symmetry. *Phys. Rev. C* **2015**, *92*, 025201; Erratum in *Phys. Rev. C* **2017**, *95*, 059903. [CrossRef]
20. Mukherjee, A.; Steinheimer, J.; Schramm, S. Higher-order baryon number susceptibilities: Interplay between the chiral and the nuclear liquid-gas transitions. *Phys. Rev. C* **2017**, *96*, 025205. [CrossRef]
21. Suenaga, D. Examination of $N^*(1535)$ as a probe to observe the partial restoration of chiral symmetry in nuclear matter. *Phys. Rev. C* **2018**, *97*, 045203. [CrossRef]
22. Takeda, Y.; Kim, Y.; Harada, M. Catalysis of partial chiral symmetry restoration by Δ matter. *Phys. Rev. C* **2018**, *97*, 065202. [CrossRef]
23. Mukherjee, A.; Schramm, S.; Steinheimer, J.; Dexheimer, V. The application of the Quark-Hadron Chiral Parity-Doublet Model to neutron star matter. *Astron. Astrophys.* **2017**, *608*, A110. [CrossRef]
24. Paeng, W.G.; Kuo, T.T.S.; Lee, H.K.; Ma, Y.L.; Rho, M. Scale-invariant hidden local symmetry, topology change, and dense baryonic matter. II. *Phys. Rev. D* **2017**, *96*, 014031. [CrossRef]
25. Marczenko, M.; Sasaki, C. Net-baryon number fluctuations in the Hybrid Quark-Meson-Nucleon model at finite density. *Phys. Rev. D* **2018**, *97*, 036011. [CrossRef]
26. Abuki, H.; Takeda, Y.; Harada, M. Dual chiral density waves in nuclear matter. *Epj Web Conf.* **2018**, *192*, 00020. [CrossRef]
27. Marczenko, M.; Blaschke, D.; Redlich, K.; Sasaki, C. Chiral symmetry restoration by parity doubling and the structure of neutron stars. *Phys. Rev. D* **2018**, *98*, 103021. [CrossRef]
28. Marczenko, M.; Blaschke, D.; Redlich, K.; Sasaki, C. Parity Doubling and the Dense Matter Phase Diagram under Constraints from Multi-Messenger Astronomy. *Universe* **2019**, *5*, 180. [CrossRef]
29. Yamazaki, T.; Harada, M. Constraint to chiral invariant masses of nucleons from GW170817 in an extended parity doublet model. *Phys. Rev. C* **2019**, *100*, 025205. [CrossRef]
30. Harada, M.; Yamazaki, T. Charmed Mesons in Nuclear Matter Based on Chiral Effective Models. *Jps Conf. Proc.* **2019**, *26*, 024001. [CrossRef]
31. Marczenko, M.; Blaschke, D.; Redlich, K.; Sasaki, C. Toward a unified equation of state for multi-messenger astronomy. *Astron. Astrophys.* **2020**, *643*, A82. [CrossRef]
32. Harada, M. Dense nuclear matter based on a chiral model with parity doublet structure. In Proceedings of the 18th International Conference on Hadron Spectroscopy and Structure, Guilin, China, 16–21 August 2019. [CrossRef]
33. Minamikawa, T.; Kojo, T.; Harada, M. Quark-hadron crossover equations of state for neutron stars: Constraining the chiral invariant mass in a parity doublet model. *Phys. Rev. C* **2021**, *103*, 045205. [CrossRef]
34. Marczenko, M.; Redlich, K.; Sasaki, C. Reconciling Multi-messenger Constraints with Chiral Symmetry Restoration. *Astrophys. J. Lett.* **2022**, *925*, L23. [CrossRef]
35. Minamikawa, T.; Kojo, T.; Harada, M. Chiral condensates for neutron stars in hadron-quark crossover: From a parity doublet nucleon model to a Nambu–Jona-Lasinio quark model. *Phys. Rev. C* **2021**, *104*, 065201. [CrossRef]
36. Marczenko, M.; Redlich, K.; Sasaki, C. Chiral symmetry restoration and Δ matter formation in neutron stars. *Phys. Rev. D* **2022**, *105*, 103009. [CrossRef]
37. Gao, B.; Minamikawa, T.; Kojo, T.; Harada, M. Impacts of the $\mathrm{U}(1)_A$ anomaly on nuclear and neutron star equation of state based on a parity doublet model. *Phys. Rev. C* **2022**, *106*, 065205. [CrossRef]
38. Minamikawa, T.; Gao, B.; Kojo, T.; Harada, M. Chiral restoration of nucleons in neutron star matter: Studies based on a parity doublet model. *Symmetry* **2023**, *15*, 745. [CrossRef]
39. Marczenko, M.; Redlich, K.; Sasaki, C. Fluctuations near the liquid-gas and chiral phase transitions in hadronic matter. *Phys. Rev. D* **2023**, *107*, 054046. [CrossRef]
40. Gao, B.; Yan, Y.; Harada, M. Reconciling constraints from the supernova remnant HESS J1731-347 with the parity doublet model. *Phys. Rev. C* **2024**, *109*, 065807. [CrossRef]
41. Baym, G.; Hatsuda, T.; Kojo, T.; Powell, P.D.; Song, Y.; Takatsuka, T. From hadrons to quarks in neutron stars: A review. *Rep. Prog. Phys.* **2018**, *81*, 056902. [CrossRef]
42. Baym, G.; Furusawa, S.; Hatsuda, T.; Kojo, T.; Togashi, H. New Neutron Star Equation of State with Quark–Hadron Crossover. *Astrophys. J.* **2019**, *885*, 42. [CrossRef]
43. Cromartie, H.T.; Fonseca, E.; Ransom, S.M.; Demorest, P.B.; Arzoumanian, Z.; Blumer, H.; Brook, P.R.; DeCesar, M.E.; Dolch, T.; Ellis, J.A.; et al. Relativistic Shapiro delay measurements of an extremely massive millisecond pulsar. *Nat. Astron.* **2019**, *4*, 72–76. [CrossRef]
44. Abbott, B.P.; Abbott, R.; Abbott, D.; Acernese, F.; Ackley, K.; Adams, C.; Adams, T.; Addesso, P.; Adhikari, X.; Adya, B.; et al. GW170817: Observation of Gravitational Waves from a Binary Neutron Star Inspiral. *Phys. Rev. Lett.* **2017**, *119*, 161101. [CrossRef]
45. Abbott, B.P. Multi-messenger Observations of a Binary Neutron Star Merger. *Astrophys. J. Lett.* **2017**, *848*, L12. [CrossRef]

46. Abbott, B.P.; Abbott, R.; Abbott, D.; Acernese, F.; Ackley, K.; Adams, C.; Adams, T.; Addesso, P.; Adhikari, X.; Adya, B.; et al. GW170817: Measurements of neutron star radii and equation of state. *Phys. Rev. Lett.* **2018**, *121*, 161101. [CrossRef]
47. Miller, M.; Lamb, F.K.; Dittmann, A.J.; Bogdanov, S.; Arzoumanian, Z.; Gendreau, K.C.; Guillot, S.; Harding, A.K.; Ho, W.C.G.; Lattimer, J.M.; et al. PSR J0030+0451 Mass and Radius from *NICER* Data and Implications for the Properties of Neutron Star Matter. *Astrophys. J. Lett.* **2019**, *887*, L24. [CrossRef]
48. Riley, T.E.; Watts, A.L.; Bogdanov, S.; Ray, P.S.; Ludlam, R.M.; Guillot, S.; Arzoumanian, Z.; Baker, C.L.; Bilous, A.V.; Chakrabarty, D.; et al. A *NICER* View of PSR J0030+0451: Millisecond Pulsar Parameter Estimation. *Astrophys. J. Lett.* **2019**, *887*, L21. [CrossRef]
49. Fonseca, E.; Cromartie, H.T.; Pennucci, T.T.; Ray, P.S.; Kirichenko, A.Y.; Ransom, S.M.; Demorest, P.B.; Stairs, I.H.; Arzoumanian, Z.; Guillemot, L.; et al. Refined Mass and Geometric Measurements of the High-mass PSR J0740+6620. *Astrophys. J. Lett.* **2021**, *915*, L12. [CrossRef]
50. De, S.; Finstad, D.; Lattimer, J.M.; Brown, D.A.; Berger, E.; Biwer, C.M. Tidal Deformabilities and Radii of Neutron Stars from the Observation of GW170817. *Phys. Rev. Lett.* **2018**, *121*, 091102. Erratum in *Phys. Rev. Lett.* **2018**, *121*, 259902. [CrossRef]
51. Radice, D.; Perego, A.; Zappa, F.; Bernuzzi, S. GW170817: Joint Constraint on the Neutron Star Equation of State from Multimessenger Observations. *Astrophys. J. Lett.* **2018**, *852*, L29. [CrossRef]
52. Doroshenko, V.; Suleimanov, V.; Pühlhofer, G.; Santangelo, A. A strangely light neutron star within a supernova remnant. *Nat. Astron.* **2022**, *6*, 1444–1451. [CrossRef]
53. Kubis, S.; Kutschera, M. Nuclear matter in relativistic mean field theory with isovector scalar meson. *Phys. Lett. B* **1997**, *399*, 191–195. [CrossRef]
54. Kubis, S.; Kutschera, M.; Stachniewicz, S. Neutron Stars in Relativistic Mean Field Theory with Isovector Scalar Meson. *arXiv* **1998**, arXiv:astro-ph/9802303. [CrossRef]
55. Miyatsu, T.; Cheoun, M.K.; Saito, K. Asymmetric Nuclear Matter in Relativistic Mean-field Models with Isoscalar- and Isovector-meson Mixing. *Astrophys. J.* **2022**, *929*, 82. [CrossRef]
56. Li, F.; Cai, B.J.; Zhou, Y.; Jiang, W.Z.; Chen, L.W. Effects of Isoscalar- and Isovector-scalar Meson Mixing on Neutron Star Structure. *Astrophys. J.* **2022**, *929*, 183. [CrossRef]
57. Miyatsu, T.; Cheoun, M.K.; Kim, K.; Saito, K. Massive neutron stars with small radii in relativistic mean-field models optimized to nuclear ground states. *arXiv* **2022**, arXiv:2209.02861. [CrossRef]
58. Thakur, V.; Kumar, R.; Kumar, P.; Kumar, V.; Kumar, M.; Mondal, C.; Agrawal, B.K.; Dhiman, S.K. Effects of an isovector scalar meson on the equation of state of dense matter within a relativistic mean field model. *Phys. Rev. C* **2022**, *106*, 045806. [CrossRef]
59. Liu, B.; Guo, H.; Toro, M.D.; Greco, V. Neutron stars with isovector scalar correlations. *Eur. Phys. J. A* **2005**, *25*, 293–298. [CrossRef]
60. Rabhi, A.; Providência, C.; Providência, J.D. Effect of the δ meson on the instabilities of nuclear matter under strong magnetic fields. *Phys. Rev. C* **2009**, *80*, 025806. [CrossRef]
61. Gaitanos, T.; Toro, M.D.; Typel, S.; Baran, V.; Fuchs, C.; Greco, V.; Wolter, H. On the Lorentz structure of the symmetry energy. *Nucl. Phys. A* **2004**, *732*, 24–48. [CrossRef]
62. Greco, V.; Colonna, M.; Di Toro, M.; Matera, F. Collective modes of asymmetric nuclear matter in quantum hadrodynamics. *Phys. Rev. C* **2003**, *67*, 015203. [CrossRef]
63. Liu, B.; Greco, V.; Baran, V.; Colonna, M.; Di Toro, M. Asymmetric nuclear matter: The role of the isovector scalar channel. *Phys. Rev. C* **2002**, *65*, 045201. [CrossRef]
64. Wang, S.; Zhang, H.F.; Dong, J.M. Neutron star properties in density-dependent relativistic mean field theory with consideration of an isovector scalar meson. *Phys. Rev. C* **2014**, *90*, 055801. [CrossRef]
65. Roca-Maza, X.; Viñas, X.; Centelles, M.; Ring, P.; Schuck, P. Relativistic mean-field interaction with density-dependent meson-nucleon vertices based on microscopical calculations. *Phys. Rev. C* **2011**, *84*, 054309. [CrossRef]
66. Kong, Y.K.; Minamikawa, T.; Harada, M. Neutron star matter based on a parity doublet model including the $a_0(980)$ meson. *Phys. Rev. C* **2023**, *108*, 055206. [CrossRef]
67. Mun, M.H.; Shin, I.J.; Paeng, W.G.; Harada, M.; Kim, Y. Nuclear structure in parity doublet model. *Eur. Phys. J. A* **2023**, *59*, 149. [CrossRef]
68. Meng, J.; Toki, H.; Zhou, S.G.; Zhang, S.Q.; Long, W.H.; Geng, L.S. Relativistic Continuum Hartree Bogoliubov theory for ground state properties of exotic nuclei. *Prog. Part. Nucl. Phys.* **2006**, *57*, 470–563. [CrossRef]
69. Bando, M.; Kugo, T.; Uehara, S.; Yamawaki, K.; Yanagida, T. Is the ρ Meson a Dynamical Gauge Boson of Hidden Local Symmetry? *Phys. Rev. Lett.* **1985**, *54*, 1215–1218. [CrossRef]
70. Bando, M.; Kugo, T.; Yamawaki, K. Nonlinear Realization and Hidden Local Symmetries. *Phys. Rept.* **1988**, *164*, 217–314. [CrossRef]
71. Harada, M.; Yamawaki, K. Hidden local symmetry at loop: A New perspective of composite gauge boson and chiral phase transition. *Phys. Rept.* **2003**, *381*, 1–233. [CrossRef]
72. Li, B.A.; Cai, B.J.; Xie, W.J.; Zhang, N.B. Progress in Constraining Nuclear Symmetry Energy Using Neutron Star Observables Since GW170817. *Universe* **2021**, *7*, 182. [CrossRef]
73. Garg, U.; Colò, G. The compression-mode giant resonances and nuclear incompressibility. *Prog. Part. Nucl. Phys.* **2018**, *101*, 55–95. [CrossRef]

74. Sunardi, A.; Sulaksono, A. Nuclear bubble in Sn isotope within modified relativistic mean field. *AIP Conf. Proc.* **2018**, *2023*, 020007. [CrossRef]
75. Zhao, P.W.; Li, Z.P.; Yao, J.M.; Meng, J. New parametrization for the nuclear covariant energy density functional with point-coupling interaction. *Phys. Rev. C* **2010**, *82*, 054319. [CrossRef]
76. Xia, X.W.; Lim, Y.; Zhao, P.W.; Liang, H.Z.; Qu, X.Y.; Chen, Y.; Liu, H.; Zhang, L.F.; Zhang, S.Q.; Kim, Y.; et al. The limits of the nuclear landscape explored by the relativistic continuum Hartree–Bogoliubov theory. *Atom. Data Nucl. Data Tabl.* **2018**, *121–122*, 1–215. [CrossRef]
77. Coraggio, L.; Holt, J.W.; Itaco, N.; Machleidt, R.; Sammarruca, F. Reduced regulator dependence of neutron-matter predictions with perturbative chiral interactions. *Phys. Rev. C* **2013**, *87*, 014322. [CrossRef]
78. Entem, D.R.; Machleidt, R. Accurate charge-dependent nucleon-nucleon potential at fourth order of chiral perturbation theory. *Phys. Rev. C* **2003**, *68*, 041001. [CrossRef]
79. Lim, Y.; Holt, J.W. Structure of neutron star crusts from new Skyrme effective interactions constrained by chiral effective field theory. *Phys. Rev. C* **2017**, *95*, 065805. [CrossRef]